Accepted Manuscript

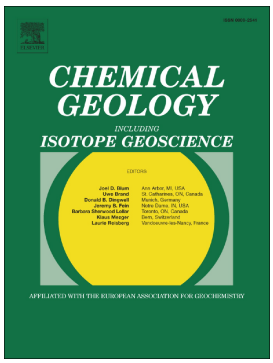

Variation in sub-arc mantle oxygen fugacity during partial melting recorded in refractory peridotite xenoliths from the West Bismarck Arc

Antoine Bénard, Alan B. Woodland, Richard J. Arculus, Oliver Nebel, Sarlae R.B. McAlpine

PII: S0009-2541(18)30116-5
DOI: doi:10.1016/j.chemgeo.2018.03.004
Reference: CHEMGE 18684

To appear in: *Chemical Geology*

Received date: 13 November 2017
Revised date: 12 February 2018
Accepted date: 1 March 2018

Please cite this article as: Antoine Bénard, Alan B. Woodland, Richard J. Arculus, Oliver Nebel, Sarlae R.B. McAlpine , Variation in sub-arc mantle oxygen fugacity during partial melting recorded in refractory peridotite xenoliths from the West Bismarck Arc. The address for the corresponding author was captured as affiliation for all authors. Please check if appropriate. Chemge(2017), doi:10.1016/j.chemgeo.2018.03.004

Variation in sub-arc mantle oxygen fugacity during partial melting recorded in refractory peridotite xenoliths from the West Bismarck Arc

Antoine Bénard[1,2†*], Alan B Woodland[3], Richard J Arculus[1], Oliver Nebel[2], Sarlae RB McAlpine[1]

[1]Research School of Earth Sciences, The Australian National University, 2601 Acton, ACT, Australia

[2]School of Earth, Atmosphere and Environment, Monash University, 3800 Clayton, VIC, Australia

[3]Institut für Geowissenschaften, Goethe Universität Frankfurt, 60438 Frankfurt am Main, Germany

[†]Present address: Institute of Earth Sciences, University of Lausanne, 1015 Lausanne, Switzerland

[*]Corresponding author email: antoine.benard@unil.ch; antoine.benard@anu.edu.au

Abstract

It is debatable whether oxygen fugacity (fO_2), the usual measure of the oxidation state of a geological system, can vary during partial melting in the Earth's mantle or not. Notably, samples of mantle peridotite recovered from lavas and pyroclastic deposits in island arcs are mostly more oxidized than those from other tectonic settings. However, the petrological history of sub-arc mantle peridotites, in particular the respective extents to which partial melting and post-melting metasomatism have controlled their fO_2 record, are elusive. It has remained unclear whether the oxidized peridotites have preserved the redox state of a melt-depleted, residual mantle wedge or not.

Here we report Mössbauer spectroscopy and EPMA measurements of Fe valence states in spinel ($Fe^{3+}/\sum Fe_{spinel}$ where $\sum Fe$ refers to $Fe^{3+}+Fe^{2+}$) in a suite of markedly unaltered, sub-arc mantle-derived, harzburgite xenoliths from the active Ritter volcano (West Bismarck Arc, Papua New Guinea). These rocks, together with similar suites from the Kamchatka and Izu-Bonin arcs, have recently been interpreted to be residues of partial melting in the mantle wedge. The $Fe^{3+}/\sum Fe_{spinel}$ decreases from 0.27±0.04 to 0.11±0.01 with increasing degrees of melt depletion in the West Bismarck sample suite, as monitored by decreasing Al_2O_3 (from 0.72 to 0.29 wt%) and modal percentage of orthopyroxene (from ~28 to ~7 wt%) in bulk rocks. Importantly, $Fe^{3+}/\sum Fe_{spinel}$ in the most melt-depleted,

orthopyroxene-poor residual samples are significantly lower (down to 0.11±0.01) than those in melt-percolated harzburgite (0.29±0.04) and dunite melt channel-cumulates (0.20±0.01) found at the same sampling sites. The calculated fO_2 in West Bismarck residual samples decreases from +1.7±0.2 to -0.5±0.2 log units relative to the synthetic fayalite-magnetite-quartz redox buffer ($\Delta\log fO_2$(FMQ)) with Al_2O_3 and orthopyroxene contents. The upper-end $\Delta\log fO_2$ for the least melt-depleted, orthopyroxene-rich residual samples are consistent with those for sub-arc mantle harzburgite xenoliths from the Kamchatka and Izu-Bonin arcs recording similar melting degrees, but also for more fertile lherzolite and harzburgite rocks from the northeastern Japan Arc. In turn, the most melt-depleted, orthopyroxene-poor residual samples have $\Delta\log fO_2$ similar to the upper bound recorded in abyssal peridotites.

Taking literature data into consideration, the fO_2 spectrum recorded by the West Bismarck sub-arc mantle peridotite suite is modelled here by a two-stage partial melting process. The first-stage oxidation state is near-buffered from lherzolite to orthopyroxene-rich harzburgite by fluxed-melting with volatile-rich, slab-derived components at ca. FMQ+0.5 to FMQ+1.5 during the generation of high-partial melting degree, picrite-boninite-andesite oxidized liquids. The second-stage oxidation state is un-buffered during second-stage melting of residual harzburgite accompanying generation of relatively low-degree partial melts such as low-Ca boninite; these preserve more variable fO_2 extending to lower values (FMQ and below) owing to the progressive removal of Fe^{3+} from their sources with increasing melting degree. The second-stage melting event likely occurs during adiabatic decompression of residual spinel harzburgite in the uppermost mantle wedge.

The data in this study supports the general hypothesis that $Fe^{3+}/\sum Fe_{spinel}$ and fO_2 of residual peridotite (and of the melts formed at equilibrium) can vary during partial melting in the Earth's mantle. These results further provide direct source evidence for the controls of various subduction zone melting processes on the oxidation state of different types of primary arc melts. Melt depletion of mantle wedge sources can result in a progressive decrease in the fO_2 of subsequent melt extracts, but only in the absence of oxidized, Si- and volatile-rich components; these are presumably derived from the subducted slab and effectively buffer fO_2 during fluxed-melting. The observed fO_2 variability in sub-arc lithospheric mantle peridotites worldwide likely reflects the combination of fluxed and adiabatic decompression melting in the mantle wedge.

Keywords

Oxidation state; oxygen fugacity; mantle wedge; sub-arc mantle; peridotite xenolith; subduction zone; island arc

1. Introduction

Subduction zones play a key role in the chemical differentiation of the Earth, and typical arc magmas, such as low-Fe (or calcalkaline) andesites, appear to be volumetrically important fractions of the Earth's upper continental crust (Taylor and White 1965; Gill 1981; Arculus 2003; Kelemen 1995; Kelemen et al. 2014; Rudnick and Gao 2014). Partial melting in the Earth's mantle overlying the subducted lithospheric plate ('slab'), referred to herein as the 'mantle wedge' for its asthenospheric portion, occurs in the presence of volatiles (C-O-H-S) derived from the slab, which exert significant controls on the physicochemical conditions of melting (Kushiro 1968; Mysen and Boettcher 1975; Gaetani and Grove 1998; Ulmer 2001; Gaetani and Grove 2003; Parman and Grove 2004; Grove et al. 2006). In this context, the oxidation state is of critical interest given the possible interplay between multi-valent, slab-derived volatile elements and the mantle wedge (e.g. Klimm et al. 2012).

The oxidation state of the Earth's mantle and melts derived therefrom, generally monitored as fO_2, is primarily controlled by Fe^{3+}-Fe^{2+} equilibria (Ballhaus 1993) coupled with the observation that mantle mineral-hosted Fe^{3+} generally behaves as a moderately incompatible element during partial melting (Bryndzia and Wood 1990; Canil et al. 1994; Mallmann and O'Neill 2009). While some studies have shown that $Fe^{3+}/\sum Fe$ (where $\sum Fe$ refers to $Fe^{3+}+Fe^{2+}$) in bulk peridotites decreases with melt extraction (Canil et al. 1994; Woodland et al. 2006), a similar effect on $Fe^{3+}/\sum Fe$ in spinel ($Fe^{3+}/\sum Fe_{spinel}$) is neither supported by global datasets (Ballhaus 1993; Canil and O'Neill 1996) nor in agreement with the results of some experimental studies (Ballhaus et al. 1991). In particular, the melt depletion signal in global datasets is frequently overprinted by the effects of post-melting metasomatism, which tend to increase fO_2 (Ballhaus 1993). Since spinel is used to calculate equilibrium fO_2 for mantle assemblages using a variety of models (O'Neill and Wall 1987; Mattioli and Wood 1988; Wood et al. 1990; Ballhaus et al. 1991), the determination of the effects of partial melting on $Fe^{3+}/\sum Fe_{spinel}$ in the residual mantle is of primary importance.

The debate on the effects of partial melting on fO_2 in the mantle is particularly relevant to subduction zones where both partial melting and recycling (or mantle 're-fertilization') processes occur. The inferred depletion of the pre-subduction protoliths of arc magma mantle sources, for

instance compared to those of mid-ocean ridge basalts (MORB; Nebel et al. 2015), could impose a relatively reduced character to melts and peridotite residues at subduction zones. On the contrary, arc magmas record more variable and generally higher oxidation states than observed in other tectonic settings (Arculus 1985; Carmichael 1991; Bézos and Humler 2005; Jugo et al. 2010; Cottrell and Kelley 2011; Evans et al. 2012; Kelley and Cottrell 2012). The origin of this more oxidized nature remains controversial. It has been proposed that recycled, volatile-rich components derived from the slab, which were originally oxidized at the Earth's surface, could impose a higher fO_2 on the mantle wedge sources of arc magmas (Arculus 1994; Kelley and Cottrell 2009; Klimm et al. 2012; Brounce et al. 2014). Alternatively, the high fO_2 of arc magmas has been suggested to derive from some redox exchange occurring during prolonged magma ascent and differentiation (Lee et al. 2005; Mallmann and O'Neill 2009). However, these models are based on indirect estimates of the oxidation state of mantle wedge source regions derived from arc lavas and their crystal-hosted glass (formerly melt) inclusions (MIs). These MIs can be strongly transformed by differentiation processes, in particular late-stage oxidation, just before and during eruption (e.g. Danyushevsky et al. 2000; Gaetani et al. 2012). Therefore, it is important to gain direct information on mantle wedge redox state, for instance by studying mantle xenoliths that have been entrained in arc magmas.

An elevated fO_2 in sub-arc mantle xenoliths has been widely recognized (Wood and Virgo 1989; Wood et al. 1990; Brandon and Draper 1996; Parkinson and Pearce 1998; Parkinson and Arculus 1999; Frost and McCammon 2008), but it remains unclear whether melting of the mantle wedge originally formed these residual sub-arc peridotites or not. In particular, the bulk SiO_2 and modal orthopyroxene enrichments in sub-arc, spinel harzburgite xenoliths compared to residual solids from the melting of fertile mantle (Herzberg 2004) are discordant. Bénard et al. (2017) showed that these orthopyroxene-rich harzburgite xenoliths are residues of sources that underwent 'fluxed-melting' by interaction with Si-rich, slab-derived components (Bénard et al. 2017). It follows that if both bulk SiO_2 content and elevated fO_2 are caused by slab-derived agents, a relationship between these two parameters might be observable in residual, sub-arc mantle xenoliths. Here we test this relationship by using Mössbauer spectroscopy and EPMA to study $Fe^{3+}/\sum Fe_{spinel}$ in harzburgite xenoliths from the sub-arc lithospheric mantle. The samples were recently recovered from the active Ritter volcano in the West Bismarck Arc (Papua New Guinea). The results are used to constrain the oxidation state evolution

during various melting processes in the mantle wedge, such as fluxed and adiabatic decompression melting.

2. Geological setting of Ritter arc volcano and its peridotite xenoliths

Samples were recovered from Ritter Volcano in the West Bismarck Arc (Papua New Guinea; PNG), located ~20 km west of New Britain (Fig. 1). The tectonic evolution of the PNG region has been controlled by the collision of the Pacific Plate with the Australian Plate during the past thirty million years; this collision commenced in the Pliocene in southeast PNG and continues today (Fig. 1a; Silver et al. 1991; Abers and McCaffrey 1994). The convergence of the two major tectonic plates has been mostly accommodated by the Solomon Islands, New Britain, and West Bismarck trench-arc systems (Fig. 1a; van Ufford and Cloos 2005). New Britain-West Bismarck overlies the subducting Solomon Sea Plate in the east, and is juxtaposed with the collided northern margin of Papua in the west.

Subduction of the Solomon Sea Plate beneath New Britain defines a clear, steep Wadati-Benioff plane, dipping at 20° until 60 km depth and at 70-75° at greater depths, and some change in azimuth and convergence rates along-strike (Fig. 1a; Cooper and Taylor 1987; Abbott et al. 1994; Wallace et al. 2004; Davidson 2005; Lindley 2006). The tectonic setting of the West Bismarck Arc is more complex because of the arc-continent collision. The Solomon Sea oceanic crust has been overridden by the collision of the Australian Plate with the South Bismarck Sea Plate, leading to the destruction of the submarine trench (Fig. 1a; Abers and McCaffrey 1988; Silver et al. 1991; Abbott et al. 1994). However, subduction persists westward with a steeply dipping remnant slab of subducted lithosphere hanging ~100 km beneath the coastal ranges of Papua and continuous along strike with the New Britain seismic zone to the east (Abers and Roecker 1991). No modern study exists but an older estimate of the depth of the sub-oceanic crust Moho in the West Bismarck Arc is ~18 km (Connelly, 1976).

The eroded subaerial edifice of Ritter, remnant from a sector collapse in 1888 AD, is located at 5.52°S, 148.12°E. The WeBiVE voyage (SS06-2007) of Australia's Marine National Facility RV *Southern Surveyor* mapped with multi-beam sonar the debris field extending northwest from Ritter located between Umboi and Sakar near the volcanic front of the arc, ~20 km west of New Britain (Fig. 1b). The peridotite xenoliths were recovered from three cinder cones, one of which is hydrothermally active, in the debris field (Fig. 1b). The host magma of the peridotites is a low-K picrite (Bénard et al.

2017). Full sample suite characterisation of the xenoliths has been documented by McAlpine (2016), and among ultramafic rocks includes pyroxenite, harzburgite, and dunite.

3. Petrological features of Ritter peridotite xenoliths in this study

Thin-section photomicrographs of representative Ritter peridotites selected for this study are provided in Figure 2. Sample selection for this study focused on 14 peridotites (10 harzburgites and 4 dunites; Table 1) from a subset described by Bénard et al. (2017). The selected Ritter peridotites in this study are subdivided into two types on the basis of their mineral textures and major element compositions: (i) residual spinel harzburgite and dunite with medium- to coarse-grained protogranular to granoblastic texture (Fig. 2a); and (ii), melt channel-cumulate dunite with fine-grained, mosaic texture (Fig. 2b and Table 1; Bénard et al. 2017).

Bénard et al. (2017) avoided Ritter peridotites containing veins and/or fine-grained, acicular olivine-orthopyroxene aggregates formed in the sub-arc lithospheric mantle (Soustelle et al. 2010; Bénard and Ionov 2012; 2013; Ionov et al. 2013; Bénard et al. in revision). A further selection was made here to exclude one sample described by Bénard et al. (2017); 63-01(1). This sample contains sieve-textured spinel (Shaw and Dingwell 2008), albeit generally limited to the very edges of the grains (Fig. A.1). Sieve texture is an indication of otherwise cryptic, sub-surface interactions with the host magma (Shaw and Dingwell 2008) that while not necessarily affecting whole-rock major elements, can still be traced with highly incompatible lithophile trace elements. Since the present study deals with $Fe^{3+}/\sum Fe$ in spinel that are highly sensitive to late-stage fluid percolation (Ballhaus 1993), samples with sieve texture were discarded in order to focus on mantle processes. However, one of the selected residual samples in particular (67-02D(7); Table 1) contains spinel-hosted MIs formed in the sub-arc lithospheric mantle (Fig. A.2; Klimm et al. 2015; Bénard et al. 2017) and is used here to characterize the effects of post-melting mantle metasomatism on $Fe^{3+}/\sum Fe_{spinel}$ and fO_2 in an arc setting.

The residual peridotites have low clinopyroxene contents (<1.5 wt%), but variable orthopyroxene modal abundances (from ~28 wt% to ~7 wt%; Table 1). They are typically enriched in SiO_2 for a given degree of melt depletion (traced by bulk Al_2O_3 or MgO contents) in comparison with the residues of melting of primitive or fertile lherzolite mantle (Herzberg 2004; Bénard et al. 2017). This geochemical feature is characteristic of sub-arc mantle peridotites in general (Herzberg 2004), and in particular, has been observed for Kamchatka (Avacha volcano; Ionov 2010; Bénard et al. 2017) and

Izu-Bonin (Torishima seamount; Parkinson and Pearce 1998) spinel harzburgites used as comparison in this study (see section 4). The SiO_2 enrichment in residual sub-arc mantle peridotites was recently modelled and interpreted as originating from fluxed-melting processes in the mantle wedge (Bénard et al. 2017). Some of the key points used by these authors to propose that the SiO_2 enrichment is a primary process (i.e. not related to post-melting metasomatism) include: (i) the residual major and trace element compositions of the peridotites and their constituent phases; (ii) the absence of positive correlations between Ni in olivine and orthopyroxene abundances in the bulk rocks; and (iii), the presence of common crystal orientations and high-temperature and low-stress slip systems, both typical of deformation under asthenospheric conditions for coarse olivine and orthopyroxene grains of residual origin (Soustelle et al. 2010, 2013). This latter feature is also illustrated in Figure 2a by the alignment of spinel in sample 67-02B(3), indicating grain sorting during plastic deformation, independently of whether relatively small euhedral grains or larger anhedral ones are involved.

High, but variable melting degrees can be inferred from the increasing bulk MgO and NiO contents in the residual Ritter peridotites (Fig. 3a). This correlates with decreasing Al_2O_3 and modal orthopyroxene contents (Fig. 3b) and also with a general increase in FeO_t (i.e. all Fe treated as Fe^{2+}) with decreasing pressure (Fig. 3c). These features collectively indicate that melting (from ~25 to ~35%; Fig. 3c) proceeded beyond clinopyroxene exhaustion in the residues through progressive dissolution of orthopyroxene (Fig. 3b), likely during decompression of spinel harzburgite from 1.5-2.5 to <1 GPa (Fig. 3c). Increasing FeO_t in residual peridotites, as is observed for those from Ritter in Figure 3c, can only be the result of melting at shallower pressure because of the expansion of the olivine phase volume at these conditions (e.g. O'Hara 1965). However, we note that the melting pressures of residual peridotites can be significantly different of those at which these rocks finally equilibrate (also in terms of fO_2; see section 5.3) in the mantle lithosphere where they are sampled by their carrier magmas (e.g. Ionov and Hofmann 2007). Spinel in the residual Ritter peridotites has generally higher Cr# (Cr/(Cr+Al)) and lower Mg# (Mg/(Mg+∑Fe)) than in abyssal peridotites (Dick and Bullen 1984; Niu and Hékinian 1997) and rare sub-arc mantle lherzolite from Japan (Ichinomegata crater; Takahashi 1980; Wood and Virgo 1989), but is comparable to that reported for other sub-arc mantle harzburgite from Torishima and Avacha (Fig. 4). Ritter peridotites, as well as those from Avacha, are commonly associated with websterite veins formed from arc picrite and high-Ca boninite melts (Bénard et al.

2016a) and orthopyroxenite veins formed by low-Ca boninite melts (Bénard and Ionov 2012; 2013; Bénard et al. in revision).

The melt channel-cumulate dunites contain no detectable orthopyroxene, but may have small amount of clinopyroxene (<0.5 wt%; Table 1). Spinel in the melt channel-cumulate dunite occurs as relatively small euhedral grains only, which are homogeneously distributed in the olivine matrix (Fig. 2b). The bulk rock compositions of these peridotites plot clearly outside mantle melting trends, for instance in having significantly lower NiO contents than expected for a given MgO content (Fig. 3a). Spinel grains in melt channel-cumulate dunites are characterised by generally higher Cr# and lower Mg# than in the residual Ritter peridotites (Fig. 4).

4. Sample selection from the literature

We primarily compare the new samples from Ritter to a selection of sub-arc mantle harzburgites of residual origin from Izu-Bonin (Parkinson and Pearce 1998) and Kamchatka (Ionov 2010). These sub-arc mantle rocks were selected from the literature because (i) they constitute the largest suites reported so far; (ii) their petrological features are highly comparable to those from Ritter residual peridotites (Bénard et al. 2017); and (iii), their $Fe^{3+}/\sum Fe_{spinel}$ were investigated using the same techniques as in this study (Parkinson and Pearce 1998; Bénard et al. 2016b). Arc-front Kamchatka samples include 7 spinel harzburgites (Av1, Av2, Av3, Av6, Av8, Av11, and Av15; Ionov 2010; Bénard et al. 2016b) from Avacha stratovolcano brought to the surface during eruptions <7000 years B.P. in low-K andesite and basaltic andesite hosts. The $Fe^{3+}/\sum Fe_{spinel}$ dataset for Avacha in this study and in Bénard et al. (2016b) is a selection from a larger one, which will be reported in future publications. Forearc Izu-Bonin samples include 5 spinel harzburgites from Torishima seamount (18R1(64-71), 18R1(119-124), 45R1(101-106), 45R2(33-38), and 45CC(7-10)) originally described by Parkinson and Pearce (1998). Torishima is a sediment-mantled, serpentine mud seamount (Parkinson and Pearce 1998). The full data set for depleted harburgite and dunite is further compared to that for more fertile spinel lherzolite xenoliths from Ichinomegata (IM8701, IM8702, IM8703, and IM8705; Wood and Virgo 1989) to assess the effects of fluxed-melting on fO_2. Original fO_2 datasets for Torishima and Ichinomegata samples were recalculated as per the Ritter samples in this study (see section 5); these results are presented in the supplementary Table A.1 in the online version of this paper.

In this study, we decided not to compare systematically our $Fe^{3+}/\sum Fe_{spinel}$ results with those obtained on samples from continental arcs (Canil et al. 1990; Brandon and Draper 1996). Owing to the variability of settings where continental lithospheric mantle may form (Ionov and Hofmann 2007) and its large fO_2 range (Frost and McCammon 2008), it appears to us unreasonable to compare systematically $Fe^{3+}/\sum Fe_{spinel}$ variations amongst mantle lithosphere sections in intra-oceanic and continental arcs (only shortly discussed in section 7.4), as the petrological histories of their original, pre-subduction protoliths may differ significantly. In particular, the pre-subduction protoliths of intra-oceanic arc mantle sources has likely formed at mid-ocean ridges (Parkinson and Pearce 1998; Ionov 2010; Bénard et al. 2017) for which oxidation state and other petrological features (e.g. pressure-temperature of melting) are relatively well constrained from studies of MORB and abyssal peridotites (Bryndzia and Wood 1990; Bézos and Humler 2005; Cottrell and Kelley 2011). For similar reasons, mantle peridotites from ophiolites with variable partial melting origins (Solomon; Parkinson and Arculus 1999) were excluded. Finally, sub-arc mantle xenoliths strongly modified by post-melting processes with unclear origins (Vanuatu, Grenada, and South Sandwich peridotites; Barsdell and Smith 1989; Pearce et al. 2000; Parkinson et al. 2003) or with $Fe^{3+}/\sum Fe_{spinel}$ determined solely by stoichiometric calculations (Japan, Lihir, and Klyuchevskoy peridotites; Johnson et al. 1996; McInnes et al. 2001; Ionov et al. 2013) were not considered here. The latter choice was guided by the observation that the differences in $Fe^{3+}/\sum Fe_{spinel}$ between stoichiometric calculations and Mössbauer measurements are large and random, which prevent reasonable comparison (see section 5.1 and previous stoichiometric calculations for Ritter peridotites by Bénard et al. 2017).

5. Analytical methods and fO_2 calculations

5.1 Electron-probe micro-analysis

Major element abundances in minerals were determined by electron-probe micro-analysis (EPMA) on a JXA-8900 superprobe at the Institut für Geowissenschaften, Goethe Universität (Frankfurt am Main, Germany). Measurements were made with an accelerating voltage of 15 kV, a ~3 µm spot diameter, and a beam current of 20 nA. Data were collected with normal counting times of 20-40 s on peak and 15-40 s on background (depending on the element considered). In addition, $Fe^{3+}/\sum Fe_{spinel}$ was determined in some samples (63-01(4), 67-02D(1), 67-02D(7), 67-02E(6), 62-01(2), and 62-02(4);

Table 1) at Goethe Universität by using a set of five secondary spinel standards for which $Fe^{3+}/\sum Fe$ had been previously determined by Mössbauer spectroscopy, following the procedure outlined by Wood and Virgo (1989). Corrections to the $Fe^{3+}/\sum Fe$ calculated using spinel stoichiometry were not large, but varied from -0.01 to -0.04 (overestimation) between measurement sessions. This demonstrates the danger of deriving Fe^{3+} in spinel by stoichiometry without using secondary standards as a check, since systematic differences between samples can erroneously be introduced (e.g. Davis et al. 2017). Errors in $Fe^{3+}/\sum Fe_{spinel}$ are ±0.025 (Woodland et al. 1992, 1996).

Corrected $Fe^{3+}/\sum Fe_{spinel}$ and secondary spinel standard analyses are presented in Tables 1 and A.2. All Ritter samples contain spinel with homogeneous major element composition (see section 6) with the notable exception of 67-02D(7), which contains spinel-hosted MIs. We have found these MIs formed during the percolation of their parental melts in the sub-arc lithospheric mantle, which induced the formation of halos around the inclusions with strongly modified spinel composition (Fig. A.2; Klimm et al. 2015; Bénard et al. 2017). For sample 67-02D(7), only flat portions of EPMA profiles, away from MIs, were considered in this study (Fig. A.2 and Table A.2).

5.2 Mössbauer spectroscopy

For most samples, $Fe^{3+}/\sum Fe$ in spinel was determined by Mössbauer spectroscopy at Goethe Universität on handpicked clean separates following the method outlined in Uenver-Thiele et al. (2014). Handpicked spinel separates (13-57 mg) were first washed in HF (~24 h) and dilute HCl (~5 h) to remove any silicate material or secondary magnetite from the grain boundaries. Each clean separate was ground under acetone, mixed with a small amount of sugar and packed into a pre-drilled hole in a 1 mm thick Pb disc that was subsequently closed on both sides with tape. The sample diameter was calculated so that absorber thicknesses remained 5 $mg \cdot cm^{-2}$ Fe to avoid potential saturation effects (Woodland et al. 2006).

Spectra were obtained at room temperature with the spectrometer operating in transmission and constant velocity mode using a nominal 50 mCi ^{57}Co source imbedded in a Rh matrix. The velocity scale of ±5 $mm.s^{-1}$ was calibrated relative to α-Fe. Mirror-image spectra were collected over 512 channels and folded together using the NORMOS software package (Wissel Elektronik GmbH, Germany). The spectral model for spinel employed two doublets with pseudo-Voigt peak shape for the Fe^{2+} component and a single Lorentzian doublet for Fe^{3+} (Woodland et al. 2006). The $Fe^{3+}/\sum Fe_{spinel}$

values are reported in Table 1 and the hyperfine parameters are provided in Table A.3. Uncertainties in $Fe^{3+}/\sum Fe_{spinel}$ are considered to be ±0.01 absolute.

5.3 Oxygen barometry

The oxidation state of Ritter sub-arc spinel peridotites can be estimated by using the heterogeneous equilibrium:

$$6Fe_2SiO_4 + O_2 \Leftrightarrow 6FeSiO_3 + 2Fe_3O_4 \quad (1)$$

where Fe_2SiO_4, $FeSiO_3$, and Fe_3O_4 refer to the fayalite, ferrosilite, and magnetite components in olivine, orthopyroxene, and spinel, respectively. The magnetite activity in spinel is calculated according to:

$$\log a_{Fe_3O_4}^{spinel} = \log \frac{[Fe^{2+}][Fe^{3+}]^2}{4} + \frac{1}{T}\left(406[Al]^2 + 653[Mg][Al]\right.$$

$$\left. +299[Cr]^2 + 199[Al][Cr] + 346[Mg][Cr]\right) \quad (2)$$

with fO_2 further determined in log units referenced to the synthetic fayalite-magnetite-quartz redox buffer (FMQ) using the Nell–Wood (Nell and Wood 1991) calibration for reaction (1) as follows:

$$\Delta \log fO_2(FMQ)_{P,T} = \log fO_2(FMQ)_{P,T} + \frac{220}{T} + 0.35 - \frac{0.0369P}{T}$$

$$-12\log X_{Fe}^{olivine} - \frac{2620}{T}\left(X_{Mg}^{olivine}\right)^2 + 3\log\left(X_{Fe}^{M1}X_{Fe}^{M2}\right)^{orthopyroxene} + 2\log a_{Fe_3O_4}^{spinel} \quad (3)$$

(Wood et al. 1990) where P, T, and X respectively refer to pressure, temperature, and mole or atomic fraction. Oxybarometers including spinel activity models that do not take into account the effect of Cr (Mattioli and Wood 1988) were not used in this study, owing to the variability of spinel composition amongst the sample suites (Fig. 4).

All calculations were made using temperatures estimated from the olivine-spinel thermometer of Ballhaus et al. (1991) and an average pressure of 1.5 GPa. As mentioned in section 3, fO_2 must be examined for the pressure-temperature conditions of the equilibration of the residual peridotites in the mantle lithosphere, which can be significantly different of those at which these rocks have originally experienced partial melting processes in the asthenosphere (Fig. 3c; Ionov and Hofmann 2007). Temperatures calculated with olivine-spinel and orthopyroxene-clinopyroxene methods generally overlap within error (Table A.4; O'Neill and Wall 1987; Brey and Köhler 1990; Ballhaus et al. 1991;

Putirka 2008), but we chose the former as it gives the most consistent results whereas orthopyroxene and clinopyroxene are apparently not in Fe-Mg exchange equilibrium, likely as a consequence of the late-stage, post-melting metasomatic formation of clinopyroxene (Table A.4; Parkinson and Pearce 1998; Ionov 2010; Bénard and Ionov 2013; Bénard et al. 2017). We chose a pressure of 1.5 GPa for our calculations as this covers within ±0.5 GPa the full pressure range estimated from olivine-spinel temperatures, which gives 0.9±0.3, 1.3±0.2, 1.7±0.1, and 1.1±0.3 GPa respectively for Ritter, Avacha, Torishima, and Ichinomegata spinel peridotites. For these pressure estimates, we used densities (2.7 $g \cdot cm^{-3}$ in continental crust, 3.3 $g \cdot cm^{-3}$ in the mantle, and 2.9 $g \cdot cm^{-3}$ in oceanic crust), standard geothermal gradients (25°C·km^{-1} in continental lithosphere, 10°C·km^{-1} in the mantle, and age-dependent in oceanic lithosphere; e.g. McKenzie et al. 2005), and upper plate thicknesses and ages available in Syracuse et al. (2010) and Bénard et al. (2017). Note that the pressures equivalent to the depth of the crust Moho using these calculations are respectively estimated at 0.5, 1.0, 0.4, and 1.0 GPa for Ritter, Avacha, Torishima, and Ichinomegata.

The errors associated with fO_2 values in this study are propagated from the uncertainties on the $Fe^{3+}/\sum Fe_{spinel}$ and the olivine- and orthopyroxene-averaged compositions for each sample (Tables 1 and A.5; Bénard et al. 2017).

6. Results

The results of $Fe^{3+}/\sum Fe_{spinel}$ measurements and fO_2 calculations are given in Tables 1 and A.1. The $Fe^{3+}/\sum Fe_{spinel}$ is significantly variable from one sample to another, whether this is amongst residual peridotites or between the two subtypes (i.e. residual and melt channel-cumulate), as directly observed in the Mössbauer spectra (e.g. Fig. 5). The $Fe^{3+}/\sum Fe_{spinel}$ varies from 0.11±0.01 to 0.27±0.04 in Ritter residual peridotites and generally increases with orthopyroxene abundance, and therefore, bulk rock Al_2O_3 content (Fig 6a). Residual harzburgites with >15 wt% orthopyroxene have higher $Fe^{3+}/\sum Fe_{spinel}$ (0.14±0.01 to 0.27±0.04), which is similar to that found in Torishima and Avacha harzburgites (up to 0.30±0.01; Fig. 6a; Parkinson and Pearce 1998; Bénard et al. 2016b). The $Fe^{3+}/\sum Fe_{spinel}$ in more fertile lherzolite and harzburgite from Ichinomegata (0.26-0.32, n=4; Wood and Virgo 1989) also overlaps with this upper range. The $Fe^{3+}/\sum Fe_{spinel}$ for melt-percolated sample 67-02D(7) (0.29±0.04; Fig. 6a), and for the dunite melt channel-cumulates (0.19±0.03 to 0.21±0.03; Fig. 6a), are both significantly

higher than observed for residual peridotites with <15 wt% orthopyroxene (from 0.11±0.01 to 0.17±0.01; Fig. 6a).

The $\Delta\log fO_2$ recorded by Ritter residual peridotites varies from FMQ-0.5 to ~FMQ+1.7 with 7 to 28 wt% modal orthopyroxene (Fig. 6b). Calculations with the oxybarometer of Ballhaus et al. (1991) systematically give lower fO_2 values compared to those using the method of Wood et al. (1990) (Tables 1 and A.1), which is consistent with the results of previous studies (e.g. Davis et al. 2017). The upper fO_2 range for residual harzburgites with >15 wt% modal orthopyroxene is comparable to that observed at Torishima and Avacha, as well as that reported for more fertile rocks from Ichinomegata (FMQ to FMQ+1; Fig. 6b and Table A.1). In turn, the lower fO_2 range for residual peridotites with <15 wt% modal orthopyroxene is comparable to the upper bound found in abyssal mantle rocks (Fig. 6b and Table A.1; Bryndzia and Wood 1990). Despite its relatively low orthopyroxene content (13 wt%; Table 1), the melt-percolated sample 67-02D(7) records an elevated $\Delta\log fO_2$ value of FMQ+1.4 (Fig. 6b).

7. Discussion

7.1 Crystal-chemical and mineralogical controls on the oxidation state of sub-arc mantle peridotites

The potential controls exerted by spinel crystal-chemistry on $Fe^{3+}/\sum Fe_{spinel}$ and fO_2 variations must be evaluated, together with their relationships with other geochemical features, before any interpretation or modelling of the driving petrological processes can be made. It is known that Fe^{3+}-Cr substitutions are energetically more favourable than Al^{3+}-Cr in spinel, which can lead to positive $Fe^{3+}/\sum Fe$ vs. Cr correlations in residual mantle spinel (Woodland et al. 1992; Canil and O'Neill 1996). Furthermore, Cr content in spinel has also been inferred to play a key role into the equilibrium partitioning of Fe^{3+} between spinel and clinopyroxene in lithospheric mantle rocks (Woodland et al. 2006), though the latter phase is a very minor component of Ritter harburgites and dunites (<1.5 wt% modal clinopyroxene; Table 1; Bénard et al. 2017). The magnetite activity-composition relationships in the fO_2 calculations in this study take into account the effects of variable spinel composition, though this does not preclude an $Fe^{3+}/\sum Fe_{spinel}$ (expressed by the $[Fe^{2+}][Fe^{3+}]^2$ term in equation 2) being primarily controlled by a spinel compositional parameter during melting or cooling of the residual mantle peridotites. However, a plot of $Fe^{3+}/\sum Fe_{spinel}$ vs. $Cr\#_{spinel}$ reveals that no correlation exists between the two for Ritter peridotites (Fig. 7a); this is also the case when $Cr/(Cr+Al+Fe^{3+})_{spinel}$ is considered (Table

1). Furthermore, the absence of a positive relationship in this regard is also apparent for Avacha, Torishima, and Ichinomegata peridotites (Fig. 7a and Table A.1). We note Ritter peridotites should be the most promising for establishing a relationship between $Fe^{3+}/\sum Fe_{spinel}$ and any other spinel crystal-chemical parameter, as they are those which display the greatest variability in spinel composition (Fig. 4); the present data set therefore suggests that no crystal-chemical effect could have controlled the $Fe^{3+}/\sum Fe_{spinel}$ and fO_2 trends in this study (Fig. 6).

Bulk peridotite mineralogy could be important in controlling $Fe^{3+}/\sum Fe_{spinel}$ or fO_2 variations. Sub-arc mantle peridotites from Ritter, Avacha, and Torishima are all clinopyroxene-poor, spinel harzburgite and dunite (Parkinson and Pearce 1998; Ionov 2010; Bénard et al. 2017), contrasting for instance with the petrological features most commonly observed in abyssal peridotites (Figs 3, 4, and 6), but also in the continental mantle lithosphere (Ionov and Wood 1992; Uenver-Thiele et al. 2014). Clinopyroxene contains significant amounts of Fe^{3+} (Woodland et al. 2006) but the absence of relationship between clinopyroxene modal abundances and $Fe^{3+}/\sum Fe_{spinel}$ or fO_2 for Ritter peridotites (Table 1), indicates that post-melting metasomatism through the formation of minor, late-stage clinopyroxene in these rocks exerts no control on the trends determined in this study (Fig. 6).

After spinel and clinopyroxene, orthopyroxene contains a substantial part of the bulk-rock Fe^{3+} budget in mantle peridotites, especially when this silicate mineral is abundant (Woodland et al. 2006). Therefore, assuming a constant bulk $Fe^{3+}/\sum Fe$ for all Ritter peridotites in this study, the depletion in orthopyroxene should be correlated with an increase in $Fe^{3+}/\sum Fe_{spinel}$ to maintain mass balance constraints, which is the opposite of what is observed (Fig. 6a and Table 1). In turn, the relative 'redox sensivity' (i.e. the response of fO_2 to the alteration of the bulk Fe_2O_3 of a spinel peridotite) during post-melting metasomatism must be the highest for orthopyroxene-poor residual peridotites, even for small melt or fluid to rock ratios, as their silicate mineral Fe^{3+}-buffering capacity and original bulk Fe_2O_3 contents are the lowest (Fig. 6a; Admunsen and Neumann 1992; Ballhaus et al. 1993; Parkinson and Pearce 1998; Parkinson and Arculus 1999; Woodland et al. 2006). Furthermore, the dramatic differences in $Fe^{3+}/\sum Fe_{spinel}$ and fO_2 between the orthopyroxene-poor (and low-Al_2O_3; Fig. 3b and Table 1) residual peridotites and the melt channel-cumulate dunite or percolated 67-02D(7) samples, suggest that progressive orthopyroxene depletion in the former group is not the consequence of late-stage, reactive dissolution of this mineral during melt- or fluid-rock interaction in the sub-arc mantle lithosphere (Fig. 6b). Those late-stage transformations are in fact not only typically

accompanied by oxidation of spinel (Amundsen and Neumann 1992; Ballhaus 1993), but also by modifications of the major element composition of this mineral (Parkinson and Pearce 1998; Parkinson and Arculus 1999); both of these effects are absent in the residual orthopyroxene-poor peridotites examined in this study (Figs 4 and 6). More generally, the silica-rich nature of the melts rarely found in the studied sub-arc mantle peridotites prevents orthopyroxene dissolution reactions (Ionov et al. 2011; Bénard and Ionov 2012; 2013; Bénard et al. 2017).

7.2 Pressure and temperature controls on the oxidation state of sub-arc mantle peridotites

Variations in the pressure-temperature conditions of melting or sub-solidus re-equilibration could be other possible factors controlling the equilibrium Fe^{3+}-Fe^{2+} distribution amongst peridotitic phases, and ultimately, the $Fe^{3+}/\sum Fe_{spinel}$ and fO_2 trends in this study (Fig. 6). However, an uncertainty of ±1 GPa, which adequately encompasses the 1.5 GPa we used in equation (3) to represent a 0.5-2.5 GPa range for the original formation by partial melting of residual sub-arc mantle peridotites (Fig. 3c), has been shown to translate in an error of only ca. ±0.3 logfO_2 unit (Woodland et al. 2006). This is further confirmed by the results in this study with calculated pressure-related variations of 0.3-0.4 logfO_2 unit per gigapascal, which can not account for the 2 log-unit difference in fO_2 between orthopyroxene-rich and orthopyroxene-poor residual peridotites from Ritter (Fig. 6b). However, it is important to keep in mind that we have calculated fO_2 for sub-solidus temperature conditions using equation (3) in this study. We have estimated the last pressure of equilibration (sub-solidus conditions in the mantle lithosphere) recorded in sub-arc mantle peridotites from their olivine-spinel temperatures to have ranged from 1 to 2 GPa (see section 5). Therefore, the small range of sub-solidus equilibration pressures for the Ritter harzburgite-dunite collection taken alone or together with all the sub-arc spinel peridotites considered in this study cannot be responsible for the observed fO_2 variations (Fig. 6b). In particular, we note that all orthopyroxene-rich residual peridotites from the sub-arc mantle have very similar fO_2 (Fig. 6b) despite different implied sub-solidus pressures of equilibration (see section 5).

Sub-arc mantle harzburgite and dunite of residual origin are highly melt-depleted rocks, and were originally formed by partial melting at high temperatures above 1200°C (Parkinson and Pearce 1998; Ionov 2010; Bénard et al. 2017). In contrast, temperatures of sub-solidus re-equilibration are particularly low for the Ritter peridotites examined for this study (down to 700°C; Table 1). However, redox equilibrium has been demonstrated between spinel and pyroxenes, even in low-temperature

massif lherzolites (Woodland et al. 2006). It has also been shown that mantle cooling has little influence on shifting fO_2 values, as these latter follow a trend essentially parallel to the FMQ redox buffer during such a process (Woodland et al. 1996; Parkinson and Arculus 1999). Furthermore, previous studies have suggested that the effects of the intrinsic uncertainties in the determination of equilibration temperatures (typically within ±100°C or less) on fO_2 are generally small (O'Neill and Wall 1987; Woodland et al. 1996; Parkinson and Arculus 1999). Variations of ca. ±100°C in the equilibration temperatures of mantle-derived xenoliths (Tables 1 and A.1) translate into relatively small shifts of ~0.15 logfO_2 unit (Woodland et al. 1992; Woodland et al. 2006); these are even as low as 0.01-0.02 logfO_2 units as calculated in this study.

Both pressure- and temperature-related uncertainties are either overlapped by the 'bulk' errors we calculate for fO_2 and/or the natural variability of this parameter amongst Ritter samples (Fig. 6b). Therefore, the effects of low-temperature on Fe^{3+}-Fe^{2+} disequilibrium and variable melting or sub-solidus re-equilibration conditions in a given peridotite set and amongst Ritter, Avacha, Torishima, and Ichinomegeta suites can both be neglected. This view is further supported, for instance, by the lack of correlation between equilibration temperatures and $Fe^{3+}/\sum Fe_{spinel}$ or fO_2 for sub-arc mantle peridotites (Fig. 7b and Tables 1 and A.1).

7.3 Modelling $Fe^{3+}/\sum Fe_{spinel}$ and fO_2 in residues and primary melts during partial melting

7.3.1 Partial melting with buffered fO_2

In order to further understand the nature of partial melting processes reflected by the $Fe^{3+}/\sum Fe_{spinel}$ and fO_2 variations in this study and the literature (Fig. 6), we first use the thermodynamic parameterization in pMELTS (Ghiorso et al. 2002) to simulate partial melting with buffered fO_2. A hybridized melting source that can account for the global observation that SiO_2-enriched peridotite residues form the sub-arc mantle lithosphere was recently investigated by Bénard et al. (2017); we use the same source major element composition as these authors and simulate partial melting at a fixed averaged logfO_2 of FMQ+0.7.

When investigating partial melting using pMELTS with variable bulk H_2O contents in the system as in Bénard et al. (2017) (0.01, 0.05, and 0.1 wt% H_2O), the mineralogy of sub-arc mantle peridotites worldwide can be reproduced by 15-25% melting for the lherzolite from Ichinomegata

(Takahashi 1980) and 30-50% melting for the residual spinel harzburgite and dunite from Ritter, Avacha, and Torishima (Fig. 8a; Parkinson and Pearce 1998; Ionov 2010; Bénard et al. 2017). We first note that these results are consistent with previous estimates of the degree of partial melting experienced by sub-arc mantle peridotites of residual origin on the basis of bulk Al_2O_3 content (Ionov 2010; Bénard et al. 2017). The results of our pMELTS models further indicate that melting of a source at fixed fO_2 is an efficient process for limiting variations of $Fe^{3+}/\sum Fe$ in residual spinel (Fig. 8b). Although expected, this result directly illustrates that buffering of the oxidation state by open-system melting is necessary to explain the presence of similarly oxidized spinel lherzolite and harzburgite residues in the sub-arc mantle. However, this cannot be the situation for the trend of decreasing $Fe^{3+}/\sum Fe_{spinel}$ and fO_2 with orthopyroxene contents observed in Ritter residual peridotites (Fig. 8b and c).

7.3.2 Partial melting with un-buffered fO_2

In order to simulate the potential effects of partial melting on $Fe^{3+}/\sum Fe_{spinel}$ when fO_2 is un-buffered, we use Fe^{3+}-Fe^{2+} partitioning models. For this purpose, we apply the experimentally-determined partitioning coefficients for Fe^{3+} and Fe^{2+} between a phase j and melt (respectively defined as $D_{Fe^{3+}}^{j/melt}$ and $D_{Fe^{2+}}^{j/melt}$) of Mallmann and O'Neill (2009) to the non-modal melting equations of Shaw (1970) for the concentrations in residues formed by batch and fractional partial melting. For instance in the case of Fe^{3+} concentrations, these are respectively given by:

$$\left[Fe^{3+}\right]^{residue} = \left(\frac{\sum_j x_j^{source} D_{Fe^{3+}}^{j/melt} - F\sum_j p_j^{source} D_{Fe^{3+}}^{j/melt}}{1-F}\right)\left(\frac{\left[Fe^{3+}\right]^{source}}{\sum_j x_j^{source} D_{Fe^{3+}}^{j/melt} + F\left(1-\sum_j p_j^{source} D_{Fe^{3+}}^{j/melt}\right)}\right) \quad (4)$$

and

$$\left[Fe^{3+}\right]^{residue} = \frac{\left[Fe^{3+}\right]^{source}}{1-F}\left(1-F\frac{\sum_j p_j^{source} D_{Fe^{3+}}^{j/melt}}{\sum_j x_j^{source} D_{Fe^{3+}}^{j/melt}}\right)^{\frac{1}{\sum_j p_j^{source} D_{Fe^{3+}}^{j/melt}}} \quad (5)$$

where x and p are the original (source) phase proportions and melting coefficients for phase j, and F is the melt fraction. The $Fe^{3+}/\sum Fe_{spinel}$ in the harzburgite residues are then calculated by mass balance according to:

$$\left[Fe^{3+}\right]^{residue} = x^{olivine}\left[Fe^{3+}\right]^{olivine} + x^{orthopyroxene}\left[Fe^{3+}\right]^{orthopyroxene} + x^{spinel}\left[Fe^{3+}\right]^{spinel} \quad (6)$$

re-written as:

$$\left[Fe^{3+}\right]^{spinel} = \frac{\left[Fe^{3+}\right]^{residue}}{x^{olivine}\left(\frac{D^{olivine/melt}_{Fe^{3+}}}{D^{spinel/melt}_{Fe^{3+}}}\right) + x^{orthopyroxene}\left(\frac{D^{orthopyroxene/melt}_{Fe^{3+}}}{D^{spinel/melt}_{Fe^{3+}}}\right) + x^{spinel}} \quad (7),$$

and in the same way for Fe^{2+}.

Because of the presence of minor clinopyroxene in Ritter spinel harzburgite and dunite (Table 1), phase proportions in the models can be calculated using hydrous melting reactions:

$$0.51orthopyroxene + 0.62clinopyroxene + 0.12spinel \Rightarrow 0.25olivine + 1melt \quad (8)$$

and

$$1.25orthopyroxene \Rightarrow 0.25olivine + 1melt \quad (9)$$

from the experimental studies of Gaetani and Grove (1998) and Parman and Grove (2004), respectively. Coupling these melting reactions allows us to take into account the effects of mineral suppression in residual mantle on isobaric melt productivity (Hirschmann et al. 1999). In the Fe^{3+}-Fe^{2+} partitioning models presented here, however, the harzburgite source modal compositions are re-normalized to clinopyroxene-free as this mineral certainly formed post-melting (Parkinson and Pearce 1998; Ionov 2010; Bénard et al. 2017), and x^{spinel} is fixed at ~1% to fit the observed modes (Tables 1 and A.4). The original harzburgite source in the partitioning models contains ~26.5 wt% orthopyroxene and ~7.57 wt% FeO_t, i.e. equivalent to one of the most oxidized and least melt-depleted residual samples, 67-02E(5) from Ritter (Table 1). The original bulk concentrations of FeO and Fe_2O_3 in the harzburgite source are ca. 7.31-7.36 and 0.21-0.27 wt% respectively, corresponding to $\Delta \log fO_2$ of ca. FMQ+1 to FMQ+1.35, according to calculations at 1 GPa and sub-solidus conditions using pMELTS.

The relationships between F and orthopyroxene content of the residues are consistent among models using equations (8) and (9) and pMELTS calculations with F=2-22% (Fig. 9a). The Fe^{3+}-Fe^{2+} partitioning models show that when melting proceeds, Fe^{3+} is more extensively extracted than Fe^{2+}, producing residues with lower $Fe^{3+}/\sum Fe$ than in the original source (Fig. 9b). This is consistent with

observations for bulk peridotites, experiments, and previous models using a similar approach (Canil et al. 1994; Woodland et al. 2006; Mallmann and O'Neill 2009). Batch and fractional melting trends define broad $Fe^{3+}/\sum Fe_{spinel}$ ranges that are consistent with Ritter residual peridotite data for F~2-17% (Fig. 9c).

7.4 Implications for the origins of fO_2 variations amongst mantle-derived spinel peridotites

A key result of our study is the observation that the upper $\Delta \log fO_2$ range of ca. FMQ+0.5 to FMQ+1.5 for residual spinel harzburgites with >15 wt% modal orthopyroxene (or with >0.4 wt% bulk Al_2O_3, i.e. the least melt depleted samples) from Ritter is consistent with that found in similar rocks from Avacha, Torishima, and Ichinomegata (Fig. 6b). This upper $\Delta \log fO_2$ range (Fig. 6b) indicates significantly more oxidized conditions than recorded by most mantle peridotite samples from other tectonic settings, and is in line with results of additional studies of subduction-related mantle peridotites (Fig. 10; Canil et al. 1990; Brandon and Draper 1996; Parkinson and Arculus 1999; Pearce et al. 2000; McInnes et al. 2001; Parkinson et al. 2003; Ionov et al. 2013). Exceptions to this general observation, however, include portions of the sub-continental lithospheric mantle that have been extensively metasomatized and concomitantly oxidized (e.g. Uenver-Thiele et al. 2014; 2017).

A further advantage of our data set is the demonstration that fO_2 variations in residual sub-arc mantle peridotites can be decoupled from the effects of late-stage, post-melting metasomatism (Fig. 6). Taking into account only the additional studies of subduction-related mantle peridotites where $Fe^{3+}/\sum Fe_{spinel}$ was determined by Mössbauer spectroscopy and/or precise EPMA analyses (Canil et al. 1990; Brandon and Draper 1996; Parkinson et al. 2003), a larger $\Delta \log fO_2$ range than FMQ+0.5 to FMQ+1.5 is found, with values down to FMQ-1, i.e. similar to those found in abyssal peridotites (Fig. 10; Bryndzia and Wood 1990). The trends in Figure 6 are most likely controlled by partial melting, in particular because they are consistent with a decrease in Al_2O_3 in bulk rocks (Fig. 3b), which is one of the most reliable indicators of the degree of partial melting experienced by residual mantle peridotites such as those derived from sub-arc regions (Ionov 2010). Our models further suggest that partial melting in the Earth's mantle is able to vary $Fe^{3+}/\sum Fe_{spinel}$ in residual peridotites (Fig. 9c), and consequently fO_2, in agreement with the well constrained, moderately incompatible behaviour of Fe^{3+} (Canil et al. 1994; Woodland et al. 2006; Mallmann and O'Neill 2009). To a first order therefore, the

fO_2 range in residual sub-arc mantle peridotites worldwide can be explained by variable degrees of melt extraction (Fig. 10).

Our results show that fO_2 variation in residual sub-arc mantle peridotites can be coupled with mineralogical mode fluctuations, such as variable orthopyroxene contents that are strongly related to the mechanisms of partial melting and re-fertilization, i.e. metasomatism occurring before or during melting, at subduction zones (Figs 3 and 6; Bénard et al. 2017). The orthopyroxene-rich Ritter peridotite data in this study demonstrates a different type of melting regime compared to that at mid-ocean ridges (Fig. 6; Bryndzia and Wood 1990), where interaction with oxidized components maintains high fO_2, even at much higher melting degrees (>25-30%; 'first-stage melting'; Fig. 8b and c). The orthopyroxene-poor Ritter peridotite data, in turn, suggests that melting at subduction zones can also proceed further and without the ingress of oxidized components ('second-stage melting'; Fig. 8b and c). The nature and roles of these partial melting processes in the mantle wedge are discussed in the final section below.

7.5 Implications for fO_2 evolution during partial melting processes in the mantle wedge

Results in this study have implications for the oxidation state of some primary arc melts generated in equilibrium with variably depleted, sub-arc mantle harzburgite and dunite of residual origin. In particular, whereas primary melts equilibrated at buffered fO_2 likely display limited liquidus $Fe^{3+}/\sum Fe_{spinel}$ variations (Fig. 8b), those produced by un-buffered, batch and fractional melting of relatively oxidized harzburgite will likely display a wide range in apparent fO_2 (Fig. 9c). For instance, primary arc melts produced in equilibrium with the least melt-depleted and most oxidized residual harzburgite from Ritter will record $\Delta \log fO_2$ of ca. FMQ+0.5 to FMQ+1 or even higher (Fig. 8c). In turn, the range of primary arc melts formed by harzburgite melting and produced as a counterpart of the full spectrum of residual harzburgite-dunite from Ritter will have decreasing liquidus $Fe^{3+}/\sum Fe_{spinel}$ with increasing degree of melting, either established in the harzburgite source, or during melt formation itself, or both (Fig. 8c). This variety in $Fe^{3+}/\sum Fe$ translates into $\Delta \log fO_2$ of ~FMQ+1 down to ~FMQ-0.5, overlapping with values relevant for MORB genesis (Fig. 8c; Cottrell and Kelley 2011). Thus, our data and models suggest that a variety of partial melting processes in relation to fO_2 evolution will occur in subduction zones.

Melt types identified in equilibrium with the harzburgite-dunite range of sub-arc peridotites can be divided into two groups: (i) SiO_2-rich picrite, high-Ca boninite, and magnesian basaltic andesite (Ionov et al. 2011; Bénard et al. 2016a; Bénard et al. 2017); and (ii), low-Ca boninite (Bénard and Ionov 2012; 2013; Bénard et al. in revision). The melts from the former group formed by high degrees (F>25%) of fluxed-melting of depleted, but SiO_2-enriched lherzolite at >1-1.5 GPa, leaving an orthopyroxene-rich, spinel harzburgitic residue (Mitchell and Grove 2015; Bénard et al. 2016a; Bénard et al. 2017). The recent discovery of dissolved S^{6+} in SiO_2-rich picrite and high-Ca boninite melt inclusions (Klimm et al. 2015; Bénard et al. 2016a) constrains their $\Delta\log fO_2$ of equilibration to be above FMQ+1 at >1 GPa (Klimm et al. 2012; 2015; Matjuschkin et al. 2016). The melts from the second group are produced by lower degrees of melting (F<15%) of spinel harzburgite, presumably at <1.5 GPa (Bénard and Ionov 2012; 2013; Bénard et al. in revision).

At depths of 70±20 km beneath island arcs, i.e. roughly corresponding to the pressure estimate of 2.0±0.5 GPa for the formation of orthopyroxene-rich peridotites from Ritter, temperatures as high as 1300-1400°C (Manea et al. 2005; Syracuse et al. 2010) can lead to the formation of spinel harzburgite residues (Fig. 11a). At this depth it is likely that mantle wedge melting is largely fluxed by slab-derived components, as geophysical models indicate a thermal structure with tightened isotherms below 70 km and an average sub-arc slab depth of ~100 km (Manea et al. 2005; Syracuse et al. 2010). Assuming that there are slab-derived components rendering island arc lavas more oxidized than MORB, this relatively deep region of the mantle wedge will be the most oxidized as the result of fluxing. A fluxed-melting origin for the relatively oxidized nature of sub-arc mantle, orthopyroxene-rich harzburgite of residual origin formed at $\Delta\log fO_2$=FMQ+1±0.5 (Fig. 6b) is consistent with petrological models for these rocks (Bénard et al. 2017) and the occurrence of lherzolite at Ichinomegata with $\Delta\log fO_2$ ranging from FMQ to FMQ+1 (Wood and Virgo 1989). Our pMELTS models indicate the melting process must be redox-buffered in order for peridotites with a large range in fertility to exhibit nearly the same fO_2 (Fig. 8b and c). High primary volatile contents and the predominance of S^{6+} over S^{2-} in oxidized sub-arc mantle melt inclusions of SiO_2-rich picrite, high-Ca boninite, and magnesian basaltic andesite liquids (Klimm et al. 2015; Bénard et al. 2016a), further suggest a high fO_2 controlled by slab-derived volatiles. High valence state sulfur (i.e. S^{6+}) is likely important at this stage, considering the potential candidates that can serve as slab-derived oxidizing agents (Frost and Ballhaus 1998; Kelley and Cottrell 2009; Klimm et al. 2012; Nebel et al. 2015). During their formation, high-F liquids formed by fluxed-melting will

perhaps also undergo decompression in the hot core of the wedge, especially in steeply-dipping subduction zones such as the West Bismarck Arc, potentially leading to polybaric melt extraction with buffered $Fe^{3+}/\sum Fe_{spinel}$, followed by aggregation in shallower magmatic chambers (Fig. 11a). This scenario, here constrained by our new data on orthopyroxene-rich residual harzburgites (Fig. 6b), is also in good agreement with the range of $\Delta \log fO_2$ inferred for primitive island arc lavas (FMQ+1 to FMQ+3; Jugo et al. 2010; Evans et al. 2012).

Following extraction of high-*F*, oxidized melts formed by fluxed-melting, buoyant orthopyroxene-rich, spinel harzburgite residues will further decompress during convection towards the very shallow mantle wedge, eventually leading to harzburgite second-stage melting (Fig. 11b). The physics of liquid formation and extraction during harzburgite melting is poorly studied but certainly different from that of lherzolite because: (i) melt productivity falls after clinopyroxene exhaustion (Hirshmann et al. 1999); (ii) melt viscosity decreases with generally much higher Mg/(Si+Al+Ti) in harzburgite-derived melt (Falloon and Danyushevsky 2000; Parman and Grove 2004); (iii) the density contrast increases with host mantle at lower pressure (Stolper et al. 1981); and (iv), matrix porosity drastically increases as orthopyroxene dissolves (Liang et al. 2010). Therefore, it can be anticipated that once incipient melting occurs, oxidized harzburgite-derived melts can segregate efficiently from their mantle matrix and percolate rapidly to shallower magmatic chambers (isochemical melt decompression; Fig. 11b). The significant point here is that a large range of melt composition, both in terms of major elements and redox state (from $\Delta \log fO_2$=FMQ+1.5 down to FMQ-0.5 or lower) can be produced during adiabatic decompression of variably depleted spinel harzburgite in the shallow mantle wedge (Fig. 11b). Such a second-stage melt generation process provides a viable mechanism for the generation of relatively reduced, moderate- to low-degree, harzburgite-derived melts without further input of slab-derived components. This is consistent with the relatively low $Fe^{3+}/\sum Fe_{spinel}$ in mantle-derived, low-Ca boninite orthopyroxenite veins observed from beneath Avacha and Ritter (Bénard and Ionov 2012; 2013; Bénard et al. in revision).

The occurrence of oxidized orthopyroxene-rich and more reduced, orthopyroxene-poor spinel harzburgite-dunite residues in the sub-arc mantle lithosphere is a strong indication that both fluxed and second-stage melting occurs in the mantle wedge. This also requires the presence of small-scale convection cells (Fig. 11c) that allow both melting processes to occur in close proximity, such as those

suggested from recent geophysical models of subduction zones (see Davies et al. 2016 and references therein).

8. Conclusions

We report Mössbauer spectroscopic and precise EPMA measurements of $Fe^{3+}/\sum Fe$ in residual spinel ($Fe^{3+}/\sum Fe_{spinel}$) in a set of fresh sub-arc mantle-derived, harzburgite and dunite xenoliths from the active Ritter volcano, West Bismarck Arc, Papua New Guinea. The results are as follows:

(i) The $Fe^{3+}/\sum Fe_{spinel}$ and calculated $\Delta \log fO_2$ (at 1.5 GPa) respectively decrease from 0.27±0.04 to 0.11±0.01 and from FMQ+1.7±0.2 to FMQ-0.5±0.2 with increasing melt depletion (monitored by decreasing bulk rock Al_2O_3 and orthopyroxene contents) in residual, sub-arc mantle-derived harzburgite and dunite.

(ii) Melt-percolated harzburgite and dunite melt channel-cumulate also found at the West Bismarck sampling sites have significantly higher $Fe^{3+}/\sum Fe_{spinel}$ (respectively 0.29±0.04 and 0.20±0.01) than the most depleted (orthopyroxene-poor) residual samples.

(iii) The upper $\Delta \log fO_2$ range (ca. FMQ+0.5 to FMQ+1.5) of the least melt-depleted residual samples (orthopyroxene-rich) from West Bismarck is consistent with that previously reported for sub-arc mantle harzburgite xenoliths from Kamchatka and Izu-Bonin, which record comparable degrees of melt extraction. Similar $\Delta \log fO_2$ values also occur in more fertile lherzolite from Japan. In turn, the lower $\Delta \log fO_2$ range (ca. FMQ-0.5) of the most melt-depleted residual samples (orthopyroxene-poor) from West Bismarck is consistent with the upper bound recorded in abyssal peridotites.

(iv) Our results support the hypothesis that $Fe^{3+}/\sum Fe_{spinel}$ and fO_2 of residual peridotite (and of the melts formed at equilibrium) can vary during partial melting.

(v) A two-stage partial melting process accounts for the overall fO_2 range in residual harzburgite and dunite from West Bismarck. First, fO_2 is near-buffered by volatile-rich, slab-derived components at FMQ+0.5-FMQ+1.5 during the generation of high-degree, oxidized picrite-boninite-andesite liquids by fluxed-melting. Second, fO_2 is un-buffered during second-stage melting of residual harzburgite to produce low-degree liquids such as low-Ca boninite that record more variable fO_2 extending to lower values with increasing melting degree. The

second-stage melting event likely occurs during adiabatic decompression of residual spinel harzburgite in the uppermost mantle wedge.

(vi) This two-stage melting model is consistent with the results of previous studies of vein-forming primitive melts in sub-arc mantle peridotites and suggests the presence of small-scale convection in the mantle wedge.

Acknowledgments

We thank Fred Davis, Michel Grégoire and an anonymous reviewer for their constructive and helpful reviews. Editorial handling by Catherine Chauvel is greatly appreciated. This work was funded by grants (DP120104240 and DE120100513) to Richard J Arculus and Oliver Nebel from the Australian Research Council. Antoine Bénard and Alan B Woodland are grateful to Laura Uenver-Thiele for providing help during sample preparation for Mössbauer spectroscopy.

References

Abbott LD, Silver EA, Anderson RS, Smith R, Ingle JC, Kling SA, Haig D, Small E, Galewsky J, Sliter WS (1994). Stratigraphic constraints on the development and timing of arc-continent collision in Northern Papua New Guinea. J Sediment Res 64: 169-183

Abers GA, McCaffrey R (1988) Active deformation in the New Guinea fold-and-thrust belt: Seismological evidence for strike-slip faulting and basement-involved thrusting. J Geophys Res 93: 13332-13354

Abers GA, McCaffrey R (1994) Active arc-continent collision: Earthquakes, gravity anomalies, and fault kinematics in the Huon-Finisterre collision zone, Papua Guinea. Tectonics 13: 227-245

Abers GA, Roecker SW (1991) Deep structure of an arc-continent collision: Earthquake relocation and inversion for upper mantle P and S wave velocities beneath Papua New Guinea. J Geophys Res 96: 6379-6401

Amundsen HEF, Neumann ER (1992) Redox control during mantle/melt interaction. Geochim Cosmochim Acta 56: 2405-2416

Arculus RJ (1985) Oxidation status of the mantle: Past and present. Ann Rev Earth Planet Sci 13: 75-95

Arculus RJ (1994) Aspects of magma genesis in arcs. Lithos 33: 189-208

Arculus RJ (2003) Use and abuse of the terms calcalkaline and calcalkalic. J Petrol 44: 929-935

Ariskin AA, Nikolaev GS (1996) An empirical model for the calculation of spinel-melt equilibria in mafic igneous systems at atmospheric pressure. Contrib Mineral Petrol 123: 282-292

Ballhaus C (1993) Redox states of lithospheric and asthenospheric upper mantle. Contrib Mineral Petrol 114: 331-348

Ballhaus C, Berry RF, Green DH (1991) High pressure experimental calibration of the olivine-orthopyroxene-spinel oxygen geobarometer: implications for the oxidation state of the upper mantle Contrib Mineral Petrol 107: 27-40

Ballhaus C, Frost BR (1994) The generation of oxidized CO_2-bearing basaltic melts from reduced CH_4-bearing upper mantle sources. Geochim Cosmochim Acta 58: 4931-4940

Barsdell M, Smith IEM (1989) Petrology of recrystallized ultramafic xenoliths from Merelava volcano, Vanuatu. Contrib Mineral Petrol 102: 230-241

Bénard A, Arculus RJ, Nebel O, Ionov DA, McAlpine SRB (2017) Silica-enriched mantle sources of picrite-boninite-andesite island arc magmas. Geochim Cosmochim Acta 199: 287-303

Bénard A, Ionov DA (2012) A new petrogenetic model for low-Ca boninites: Evidence from veined sub-arc xenoliths on melt-mantle interaction and melt fractionation. Geochem Geophys Geosyst doi: 10.1029/2012GC004145

Bénard A., Ionov DA (2013) Melt- and fluid-rock interaction in supra-subduction lithospheric mantle: evidence from andesite-hosted veined peridotite xenoliths. J Petrol 54: 2339-2378

Bénard A, Le Losq C, Arculus RJ, Nebel O (in revision) Low-Ca boninite formation by second-stage melting of residual spinel harzburgite in the mantle wedge of mature subduction zones: New evidence from veined mantle xenoliths from the West Bismarck Arc. Contrib Mineral Petrol

Bénard A, Nebel O, Ionov DA, Arculus RJ, Shimizu N, Métrich N (2016a) Primary silica-rich picrite and high-Ca boninite melt inclusions in pyroxenite veins from the Kamchatka sub-arc mantle. J Petrol 10: 1955-1982

Bénard A, Woodland AB, Ionov DA, Arculus RJ, Klimm K, Nebel O. (2016b) The oxidation state of the sub-arc lithospheric mantle: New data and models. 35th International Geological Congress Abstracts

Bézos A, Humler E (2005) The $Fe^{3+}/\Sigma Fe$ ratios of MORB glasses and their implications for mantle melting. Geochim Cosmochim Acta 69: 711-725

Bird P (2003) An updated digital model of plate boundaries. Geochem Geophys Geosyst doi: 10.1029/2001GC000252

Bodinier JL, Godard M (2014) Orogenic, ophiolitic, and abyssal peridotites. In Holland H, Turekian K (eds) Treatise on Geochemistry, 2nd edn. Elsevier, Amsterdam, pp 103-167

Brandon AD, Draper DS (1996) Constraints on the origin of the oxidation state of mantle overlying subduction zones: An example from Simcoe, Washington, USA. Geochim Cosmochim Acta 69: 1739-1749

Brandon AD, Snow JE, Walker RJ, Morgan JW, Mock TD (2000) ^{190}Pt-^{186}Os and ^{187}Re-^{187}Os systematics of abyssal peridotites. Earth Planet Sci Lett 177: 319-335

Brey GP, Köhler T (1990) Geothermobarometry in four-phase lherzolites II. New thermobarometers, and practical assessment of existing thermobarometers. J Petrol 31: 1353-1378

Bryndzia LT, Wood BJ (1990) Oxygen thermobarometry of abyssal spinel peridotites: The redox state and C-O-H volatile composition of the Earth's sub-oceanic upper mantle. Am J Sci 290: 1093-1116

Brounce MN, Kelley KA, Cottrell E (2014) Variations in $Fe^{3+}/\Sigma Fe$ of Marianna arc basalts and mantle wedge fO_2. J Petrol 55: 2513-2536

Canil D, Virgo D, Scarfe CM (1990) Oxidation state of mantle xenoliths from British Columbia, Canada. Contrib Mineral Petrol 104: 453-462

Canil D, O'Neill HStC (1996) Distribution of ferric iron in some upper-mantle assemblages. J Petrol 37: 609-635

Canil D, O'Neill HStC, Pearson DG, Rudnick RL, McDonough WF, Carswell DA (1994) Ferric iron in peridotites and mantle oxidation states. Earth Planet Sci Lett 123: 205-220

Cannat M, Chatin F, Whitechurch H, Ceuleneer G (1997) Gabbroic rocks trapped in the upper mantle at the Mid-Atlantic Ridge. In Karson JA, Cannat M, Miller DJ, Elthon D (eds). Proc ODP Sci Results 153: 243-264

Carmichael ISE (1991) The redox states of basic and silicic magmas: A reflection of their source regions? Contrib Mineral Petrol 106: 129-141

Casey JF (1997) Comparison of major- and trace-element geochemistry of abyssal peridotites and mafic plutonic rocks with basalts from the MARK region of the Mid-Atlantic Ridge. In Karson JA, Cannat M, Miller DJ, Elthon D (eds). Proc ODP Sci Results 153: 181-241

Connelly JB (1976) Tectonic development of the Bismarck Sea based on gravity and magnetic modelling. Geophys J R Astr Soc 46: 23-40

Cooper P, Taylor B (1987) Seismotectonics of New Guinea: A model for arc reversal following arc-continent collision. Tectonics 6: 53-67

Cottrell E, Kelley KA (2011) The oxidation state of Fe in MORB glasses and the oxygen fugacity of the upper mantle. Earth Planet Sci Lett 305: 270-282

Danyushevsky LV (2000) Re-equilibration of melt inclusions trapped by magnesian olivine phenocrysts from subduction-related magmas: Petrological implications. Contrib Mineral Petrol 138: 68-83

Davidson JP, Hora JM, Garrison JM, Dungan MA (2005) Crustal forensics in arc magmas. J Volcanol Geotherm Res 140: 157-170

Davis FA, Cottrell E, Birner SK, Warren JM, Lopez OG (2017) Revisiting the electron microprobe method of spinel-olivine-orthopyroxene oxybarometry applied to spinel peridotites. Am Min 102: 421-435

Davies DR, Le Voci G, Goes S, Kramer SC, Wilson CR (2016) The mantle wedge's transient 3-D flow regime and thermal structure. Geochem Geophys Geosyst doi: 10.1002/2015GC006125

Dick HJB, Bullen T (1984) Chromium spinel as a petrogenetic indicator in abyssal and alpine-type peridotites and spatially associated lavas. Contrib Mineral Petrol 86: 54-76

Dick HJB, Fisher RL, Bryan WB (1984) Mineralogic variability of the uppermost mantle along mid-ocean ridges. Earth Planet Sci Lett 69: 88-106

Evans KA, Elburg MA, Kamenetsky, VS (2012) Oxidation state of subarc mantle. Geology 40: 783-786

Falloon TJ, Danyushevsky LV (2000) Melting of refractory mantle at 1.5, 2 and 2.5 GPa under anhydrous and H_2O-undersaturated conditions: Implications for the petrogenesis of high-Ca boninites and the influence of subduction components on mantle melting. J Petrol 41: 257-283

Frost BR, Ballhaus C (1998) Comment on "Constraints on the origin of the oxidation state of mantle overlying subduction zones: An example from Simcoe, Washington, USA" by A. D. Brandon and D. S. Draper. Geochim Cosmochim Acta 62: 329-331

Frost DJ, McCammon CA (2008) The redox state of Earth's mantle. Annu Rev Earth Planet Sci 36: 389-420

Gaetani GA, Grove TL (1998) The influence of water on melting of mantle peridotite. Contrib Mineral Petrol 131: 326-346

Gaetani G, Grove TL (2003) Experimental constraints on melt generation in the mantle wedge. In Eiler J (ed) Inside the Subduction Factory. American Geophysical Union Geophysical Monograph, Washington DC, 138: 107-134

Gaetani G, O'Leary JA, Shimizu N, Bucholz CE, Newville M (2012) Rapid reequilibration of H_2O and oxygen fugacity in olivine-hosted melt inclusions. Geology 40: 915-918

Ghiorso MS, Hirschmann MM, Reiners PW, Kress VC (2002) The pMELTS: A revision of MELTS for improved calculation of phase relations and major element partitioning related to partial melting of the mantle to 3 GPa. Geochem Geophys Geosyst doi: 10.1029/2001GC000217

Gill JB (1981) Orogenic andesites and plate tectonics. In El Goresy A, von Engelhardt W, Hahn T (eds) Minerals and Rocks. Springer-Verlag, Berlin, Heidelberg, New York, 390 pp

Grove TL, Chatterjee N, Parman SW, Médard E (2006) The influence of H_2O on mantle wedge melting. Earth Planet Sci Lett 249: 74-89

Grove TL, Gerlach DC, Sando TW (1982) Origin of calc-alkaline series lavas at Medecine Lake volcano by fractionation, assimilation and mixing. Contrib Mineral Petrol 80: 160-182

Herzberg C (2004) Geodynamic information in peridotite petrology. J Petrol 45: 2507-2530

Hirschmann MM, Asimow PD, Ghiorso MS, Stolper EM (1999) Calculation of peridotite partial melting from thermodynamic models of minerals and melts. III. Controls on isobaric melt production and the effect of water on melt production. J Petrol 40: 831-851

Ionov DA (2010) Petrology of mantle wedge lithosphere: New data on supra-subduction zone peridotite xenoliths from the andesitic Avacha volcano, Kamchatka. J Petrol 51: 327-361

Ionov DA, Bénard A., Plechov PY (2011) Melt evolution in sub-arc mantle: Evidence from heating experiments on melt inclusions in peridotite xenoliths from the andesitic Avacha volcano (Kamchatka, Russia). Contrib Mineral Petrol 162: 1159-1174

Ionov DA, Bénard A, Plechov PY, Shcherbakov VD (2013) Along-arc variations in lithospheric mantle compositions in Kamchatka, Russia: first trace element data on mantle xenoliths from the Klyuchevskoy group volcanoes. J Volcanol Geotherm Res 263: 122-131

Ionov DA, Hofmann AW (2007) Depth of formation of subcontinental off-craton peridotites. Earth Planet Sci Lett 261: 620-634

Ionov DA, Wood BJ (1992) The oxidation state of subcontinental mantle: oxygen thermobarometry of mantle xenoliths from central Asia. Contrib Mineral Petrol 111: 179-193

Jenner FE, O'Neill HStC, Arculus RJ, Mavrogenes JA (2010) The magnesite crisis in the evolution of arc-related magmas and the initial concentration of Au, Ag and Cu. J Petrol 51: 2445-2464

Johnson RW (1987) Large-scale volcanic cone collapse: the 1888 slope failure at Ritter volcano, and other examples from Papua New Guinea. Bull Volcanol 49: 669-679

Johnson KE, Davis AM, Bryndzia LT (1996) Contrasting styles of hydrous metasomatim in the upper mantle: An ion microprobe investigation. Geochim Cosmochim Acta 60: 1367-1385

Jugo PJ, Wilke M, Botcharnikov RE (2010) Sulfur K-edge XANES analysis of natural and synthetic basaltic glasses: Implications for S speciation and S content as function of oxygen fugacity. Geochim Cosmochim Acta 74: 5926-5938

Kelemen PB (1995) Genesis of high Mg# andesites and the continental crust. Contrib Mineral Petrol 120: 1-19

Kelemen PB, Hanghøj K, Greene AR (2014) One view of the geochemistry of subduction-related magmatic arcs, with an emphasis on primitive andesite and lower crust. In Holland H, Turekian K (eds) Treatise on Geochemistry, 2nd edn. Elsevier, Amsterdam, pp 749-805

Kelley KA, Cottrell E (2009) Water and the oxidation state of subduction zone magmas. Science 325: 605-607

Kelley KA, Cottrell E (2012) The influence of magmatic differentiation on the oxidation state of Fe in a basaltic arc magma. Earth Planet Sci Lett 329-330: 109-121

Klimm K, Bénard A, Woodland AB, Arculus RJ, Ionov DA (2015) The sulphate cycle in subduction zones. Another clue to the great oxidation event? Goldschmidt Abstracts 2015: 1622

Klimm K, Kohn SC, Botcharnikov RE (2012) The dissolution mechanism of sulphur in silicate melts. II: Solubility and speciation of sulphur in silicate melts as a function of fO_2. Chem Geol 322-323: 250-267

Kress VC and Carmichael ISE (1991) The compressibility of silicate liquids containing Fe_2O_3 and the effect of composition, temperature, oxygen fugacity and pressure on their oxidation states. Contrib Mineral Petrol 108: 82-92

Kushiro I, Syono Y, Akimoto SI (1968) Melting of a peridotite nodule at high pressures and high water pressures. J Geophys Res 73: 6023-6029

Lee CTA, Leeman WP, Canil D, Li ZXA (2005) Similar V/Sc systematics in MORB and arc basalts: Implications for the oxygen fugacities of their mantle source regions. J Petrol 46: 2313-2336

Liang Y, Schiemenz A, Hesse MA, Marc Parmentier E, Hesthaven JS (2010) High-porosity channels for melt migration in the mantle: Top is the dunite and bottom is the harzburgite and lherzolite. Geophys Res Lett doi:10.1029/2010GL044162

Lindley D (2006) Extensional and vertical tectonics in the New Guinea islands: implications for island arc evolution. Ann Geophys 49: 403-426

Mallmann G, O'Neill HStC (2009) The crystal/melt partitioning of V during mantle melting as a function of oxygen fugacity compared with some other elements (Al, P, Ca, Sc, Ti, Cr, Fe, Ga, Y, Zr and Nb). J Petrol 50: 1765-1794

Manea VC, Manea M, Kostoglodov V, Sewell G (2005) Thermal models, magma transport, and velocity anomaly estimation beneath southern Kamchatka. In Foulger GR, Natland JH, Presnall DC, Anderson DL (eds) Plates, plumes, and paradigms, Geological Scociety of America Special Paper 388: 517-536

Matjuschkin V, Blundy JD, Brooker RA (2016) The effect of pressure on sulphur speciation in mid- to deep-crustal arc magmas and implications for the formation of porphyry copper deposits. Contrib Mineral Petrol 171: 66

Mattioli GS, Wood BJ (1988) Magnetite activities across the $MgAl_2O_4$-Fe_3O_4 spinel join, with applications to thermobarometric estimates of upper mantle oxygen fugacity. Contrib Mineral Petrol 98: 148-162

McAlpine SRB (2016) A petrological study of peridotite and pyroxenite xenoliths from the West Bismarck Arc and the Tabar-Lihir-Tanga-Feni Arc, Papua New Guinea. Ph. D. thesis, Australian National University, 359 pp

McInnes BIA, Gregoire M, Binns RA, Herzig PM, Hannington MD (2001) Hydrous metasomatism of oceanic sub-arc mantle, Lihir, Papua New Guinea: petrology and geochemistry of fluid-metasomatised mantle wedge xenoliths. Earth Planet Sci Lett 188: 169-183

McKenzie D, Jackson J, Priestley K (2005) Thermal structure of oceanic and continental lithosphere. Earth Planet Sci Lett 233: 337-349

Mitchell AL, Grove TL (2015) Melting the hydrous, subarc mantle: the origin of primitive andesites. Contrib Mineral Petrol 170: 13-35

Mysen BO, Boettcher AL (1975) Melting of a hydrous mantle: I. Phase relations of natural peridotite at high pressures and temperatures with controlled activities of water, carbon dioxide, and hydrogen. J Petrol 16: 520-548

Nebel O, Sossi PA, Bénard A, Wille M, Vroon PZ, Arculus RJ (2015) Redox-variability and controls in subduction zones from an iron-isotope perspective. Earth Planet Sci Lett 432: 142-151

Nell J, Wood BJ (1991) High-temperature electrical measurements and thermodynamic properties of Fe_3O_4-$FeCr_2O_4$-$MgCr_2O_4$-$FeAl_2O_4$ spinels. Am Min 76: 405-426

Niu Y, Hékinian R (1997) Basaltic liquids and harzburgitic residues in the Garrett Transform: a case study at fast-spreading ridges. Earth Planet Sci Lett 146: 243-258

O'Hara MJ (1965) Primary magmas and the origins of basalts. Scott J Geol 1: 19-40

O'Neill HStC, Wall VJ (1987) The olivine–orthopyroxene–spinel oxygen geobarometer, the nickel precipitation curve, and the oxygen fugacity of the Earth's upper mantle. J Petrol 28: 1169-1191

Osborn EF (1959) Role of oxygen partial pressure in the crystallisation and differentiation of basaltic magmas. Am J Sci 257: 609-647

Parkinson IJ, Arculus RJ (1999) The redox state of subduction zones: insights of arc-peridotites. Chem Geol 160: 409-423

Parkinson IJ, Arculus RJ, Eggins SM (2003) Peridotite xenoliths from Grenada, Lesser Antilles Island Arc. Contrib Mineral Petrol 146: 241-262

Parkinson, IJ, Pearce JA (1998) Peridotites from the Izu-Bonin-Mariana forearc (ODP leg 125): Evidence for mantle melting and melt-mantle interaction in a supra-subduction zone setting. J. Petrol. 39: 1577-1618

Parman SW, Grove TL (2004) Harzburgite melting with and without H_2O: Experimental data and predictive modelling. J Geophys Res doi:10.1029/2003JB002566

Pearce JA, Barker PF, Edwards SJ, Parkinson IJ, Leat PT (2000) Geochemistry and tectonic significance of peridotites from the South Sandwich arc-basin system, South Atlantic. Contrib Mineral Petrol 139: 36-53

Putirka KD (2008) Thermobarometers and barometers for volcanic systems. In Putirka KD, Tepley FJ (eds) Minerals, Inclusions and Volcanic Processes. Reviews in Mineralogy and Geochemistry 69: 61-120

Rudnick RL, Gao S (2014) Composition of the continental crust. In Holland H, Turekian K (eds) Treatise on Geochemistry, 2nd edn. Elsevier, Amsterdam, pp 1-51

Shaw D (1970) Trace element fractionation during anatexis. Geochim Cosmochim Acta 34: 237-243

Shaw CSJ and Dingwell DB (2008) Experimental peridotite-melt reaction at one atmosphere: a textural and chemical study. Contrib Mineral Petrol 155: 199-214

Silver EA, Abbott LD, Kirchoff-Stein KS, Reed DL, Bernstein-Taylor B, Hilyard D (1991) Collision propagation in Papua New Guinea and the Solomon Sea. Tectonics 10: 863-874

Snow JE, Dick HJB (1995) Pervasive magnesium loss by marine weathering of peridotite. Geochim Cosmochim Acta 20: 4219-4235

Soustelle V, Tommasi A, Demouchy S, Franz L (2013) Melt-rock interactions, deformation, hydration and seismic properties in the sub-arc lithospheric mantle inferred from xenoliths from seamounts near Lihir, Papua New Guinea. Tectonophysics 608: 330-345

Soustelle V, Tommasi A, Demouchy S, Ionov DA (2010) Deformation and fluid-rock interaction in the supra-subduction mantle: Microstructures and water contents in peridotite xenoliths from the Avacha volcano, Kamchatka. J Petrol 51: 363-394

Stephens CJ (1997) Heterogeneity of oceanic peridotite from the Western Canyon Wall at MARK: resulrs from Site 920 In Karson JA, Cannat M, Miller DJ, Elthon D (eds). Proc ODP Sci Results 153: 285-303

Stolper E, Walker D, Hager BH, Hays JF (1981) Melt segregation from partially molten source regions: The importance of melt density and source region size. J Geophys Res 86: 6261-6271

Syracuse EM, van Keken PE, Abers GA (2010) The global range of subduction zone thermal models. Phys Planet Earth Int 183: 73-90

Takahashi E (1980) Thermal history of lherzolite xenoliths-I. Petrology of lherzolite xenoliths from the Ichinomegata crater, Oga peninsula, northeast Japan. Geochim Cosmochim Acta 44: 1643-1658

Taylor SR, White AJR (1965) Geochemistry of andesites and the growth of continents. Nature 208: 271-273

Uenver-Thiele L, Woodland AB, Downes H, Altherr R (2014) Oxidation state of the lithospheric mantle below the Massif Central, France. J Petrol 55: 2457-2480

Uenver-Thiele L, Woodland AB, Seitz, HM, Downes H, Altherr R (2017) Metasomatic processes revealed by trace element and redox signatures of the lithospheric mantle beneath the Massif Central, France. J Petrol 58: 395-422

Ulmer P (2001) Partial melting in the mantle wedge the role of H_2O in the genesis of mantle-derived 'arc-related' magmas. Phys Earth Planet Int 127: 215-232

van Ufford AQ, Cloos M (2005) Cenozoic tectonics of New Guinea. AAPG Bull 89: 119-140

Wallace LM, Stevens C, Silver EA, McCaffrey R, Loratung W, Hasiata S, Stanaway R, Curley R, Rosa R, Taugaloidi J (2004) GPS and seismological constraints on active tectonics and arc-continent collision in Papua New Guinea: Implications for mechanics of microplate rotations in a plate boundary zone. J Geophys Res doi: 10.1029/2003JB002481

Ward SN, Day S (2003) Ritter Island volcano—lateral collapse and the tsunami of 1888. Geophys J Int 154: 891-902

Wood BJ, Taras Bryndzia L, Johnson KE (1990) Mantle oxidation state and its relationship to tectonic environment and fluid speciation. Science 248: 337-345

Wood BJ, Virgo D (1989) Upper mantle oxidation state: Ferric iron contents of lherzolite spinels by ^{57}Fe Mössbauer spectroscopy and resultant oxygen fugacities. Geochim Cosmochim Acta 53: 1277-1291

Woodland AB, Kornprobst J, Wood BJ (1992) Oxygen Thermobarometry of orogenic lherzolite massifs. J Petrol 33: 203-230

Woodland AB, Kornprobst J, McPherson E, Bodinier JL, Menzies MA (1996) Metasomatic interactions in the lithospheric mantle: Petrologic evidence from the Lherz Massif, French Pyrenees. Chem Geol 134: 83-112

Woodland AB, Kornprobst J, Tabit A (2006) Ferric iron in orogenic lherzolite massifs and controls of oxygen fugacity in the upper mantle. Lithos 89: 221-241

Figure captions

Fig. 1 (**a**) Tectonic map of the Papua New Guinea area. The active (continuous) and presumably inactive (dashed) convergent margins are in white and the spreading centres are in black. White vectors indicate the directions of convergence with averaged relative velocities given in centimetres per year

(Bird 2003). AP, Australian Plate; CP, Caroline Plate; NB, New Britain; NBP; North Bismarck Plate; NI, New Ireland; PNG, Papua New Guinea; PP, Pacific Plate; SBP; South Bismarck Plate; SSP, South Solomon Plate; WP, Woodlark Plate; WB, West Bismarck Arc. Ritter volcano is indicated with a white star. (**b**) A multibeam sonar 30 kHz swath map of the environs of Ritter. White areas indicate the emerging lands for Umboi, Ritter, and Sakar volcanic islands. Also indicated are the sampling sites for the peridotite xenoliths in this study (white stars), located on recent cones emerging from the 1888 eruption debris deposits (light grey field; Johnson 1987; Ward and Day 2003). The cones are labelled in chronological order of dredging (Table 1). Colour is indicative of depth and ranges from shallow (red) to approximately 1000 m (blue).

Fig. 2 Photomicrograph and back-scattered electron (BSE) images of Ritter peridotite xenoliths in this study. (**a**) A residual harzburgite containing (**a-1**) small euhedral and (**a-2**) large anhedral spinel grains (both in reflected light), sometimes aligned in the rock matrix (outlined by the bold blue contour). (**b**) A melt channel-cumulate dunite containing (**b-1**) small euhedral spinel grains (BSE), always homogeneously disseminated in the rock matrix. Note the dramatic difference in texture between residual spinel harzburgite (protogranular to granoblastic) and the melt channel-cumulate spinel dunite (mosaic). Opx, orthopyroxene.

Fig. 3 Petrological features of Ritter peridotite xenoliths in this study. Plots of (**a**) NiO vs. MgO, (**b**) Al_2O_3 vs. modal orthopyroxene content, and (**c**) FeO_t (all Fe treated as Fe^{2+}) vs. Al_2O_3 contents (all in wt%) for bulk rocks of residual spinel harzburgite and dunite from Ritter in this study (blue and white diamonds). The white diamond is the melt-percolated sample 67-02D(7) (Table 1). Also shown are the melt channel-cumulate spinel dunites from the same sampling sites (white dots). The dataset in this study is compared to a selection from the published literature on Avacha (Kamchatka; yellow field; Ionov 2010; Bénard et al. 2016b) and Torishima (IcB; orange field; Parkinson and Pearce 1998) spinel harzburgite and dunite xenoliths with textural and geochemical features close to those of the residual samples from Ritter (Bénard et al. 2017). Also shown are the fields for off-craton, residual mantle beneath continents (black contour) from Ionov and Hofmann (2007) and Ionov (2010) in (**a**) and the residue evolution trends for fertile lherzolite melting (black and grey lines) from Herzberg (2004) in (**c**). The green field in (**a**) and (**c**) are abyssal peridotites (Snow and Dick 1995; Cannat et al. 1997;

Casey 1997; Stephens et al. 1997; Brandon et al. 2000), selected on the basis of demonstrated, residual NiO vs. MgO (**a**) and Cr_2O_3 vs. Al_2O_3 (Bodinier and Godard 2014) relationships and FeO_t<9 wt% (**c**) (Herzberg 2004; Bénard et al. 2017).

Fig. 4 A plot of Cr# vs. Mg# for spinel grains in Ritter peridotite xenoliths. The dataset for Ritter, Avacha, and Torishima spinel harzburgite and dunite is compared to lherzolite from Ichinomegata (Japan; grey field; Wood and Virgo 1989). Also shown are literature data for abyssal peridotites (green field; Dick and Bullen 1984; Niu and Hékinian 1997). Symbols are the same as in Figure 3.

Fig. 5 Mössbauer spectra for spinel in residual peridotite xenoliths from Ritter in this study. (**a**) A relatively oxidized and orthopyroxene-rich sample (67-02E(5); Table 1) and (**b**) a relatively reduced and orthopyroxene-poor sample (67-02E(1); Table 1). See text for description of fitting procedure. Doublets assigned to Fe^{3+} are in red and those attributable to Fe^{2+} are in blue.

Fig. 6 Results of Fe valence state measurements by Mössbauer spectroscopy for spinel in Ritter peridotites. (**a**) Plot of $Fe^{3+}/\sum Fe_{spinel}$ vs. modal orthopyroxene contents (in wt%). (**b**) Plot of the calculated (Wood et al. 1990) $\Delta \log fO_2$(FMQ) vs. orthopyroxene contents in bulk rocks (in wt%). The green field is for abyssal peridotites (B&W 1990; Bryndzia and Wood 1990). In this plot, metasomatic peridotites from Romanche and Marie Celeste fracture zones and St. Paul's Rocks are excluded from the Bryndzia and Wood (1990) fO_2 original data set. The corresponding range in modal orthopyroxene is that commonly found in abyssal peridotites (Dick et al. 1984; Bodinier and Godard 2014), as expected for fertile mantle melting below 3 GPa (Ghiorso et al. 2002; Herzberg 2004). Symbols are the same as in Figure 3.

Fig. 7 Evaluation of the crystal-chemical and sub-solidus re-equilibration condition controls on the Fe valence state for spinel in Ritter peridotites in this study. (**a**) Plot of $Fe^{3+}/\sum Fe$ vs. Cr# in spinel. (**b**) Plot of $\Delta \log fO_2$(FMQ) vs. equilibration temperature, respectively calculated with the methods of Wood et al. (1990) and Ballhaus et al. (1991).

Fig. 8 Melting models at buffered fO_2 compared to the datasets in this study and the literature. (**a**) Plot of phase proportions (in wt%) vs. melting degree (*F*, in %) for the hybridized source melting models with pMELTS (Ghiorso et al. 2002) in Bénard et al. (2017) (see text for details). The model results are compared to clinopyroxene (cpx) and orthopyroxene (opx) modal proportions in sub-arc mantle peridotites (Takahashi 1980; Parkinson and Pearce 1998; Ionov 2010; Bénard et al. 2017). Ritter peridotites are represented with a blue field (West Bismarck; Bénard et al. 2017), whereas others are as in Figures 3 and 4. (**b**) Plot of $Fe^{3+}/\sum Fe_{spinel}$ vs. *F* for the same models as in (**a**) calculated at FMQ+0.7. (**c**) Plot of $\Delta \log fO_2$(FMQ) vs. *F* with the melting degrees inferred in (**a**).

Fig. 9 Partitioning melting models for Ritter residual peridotites in this study. (**a**) Plot of modal orthopyroxene content (in wt%) vs. melting degree (*F*, in %) for a spinel harburgite source calculated with pMELTS (red line; Ghiorso et al. 2002) and melting reactions (8) and (9) (blue line). (**b**) Plot of $Fe^{3+}/\sum Fe_{residue}$ vs. orthopyroxene content (in wt%) for Fe^{3+}-Fe^{2+} partitioning models (batch, blue continuous line; fractional, blue dotted line) with a spinel harzburgite source calculated at FMQ+1 (see text for details). (**c**) Plot of $Fe^{3+}/\sum Fe_{spinel}$ vs. orthopyroxene content (in wt%) for the same models as in (**b**). Symbols are the same as in Figure 3.

Fig. 10 Calculated $\Delta \log fO_2$(FMQ) for spinel peridotite assemblages from a number of tectonic settings (modified after Frost and McCammon 2008) compared to the Ritter residual harzburgite and dunite xenoliths in this study (blue field, West Bismarck). Literature references are as follows: oceanic, Bryndzia and Wood (1990); Cottrell and Kelley (2011); massif, Woodland et al. (1992); Woodland et al. (1996, 2006); continental, Ionov and Wood (1992); subduction, Canil et al. (1990); Brandon and Draper (1996); McInnes et al. (2001); Parkinson et al. (2003). Symbols are the same as in Figures 3 and 4.

Fig. 11 Schematic representations of melt generation and fO_2 evolution models in this study. (**a**) A plot of pressure (in gigapascal) vs. $\Delta \log fO_2$(FMQ) illustrating the petrogenesis of high-*F*, relatively oxidized picrite-boninite-andesite in equilibrium with orthopyroxene-rich residual harzburgite (red field; Bénard et al. 2017). The overall schematic representation is adapted from Parkinson and Arculus (1999). Grey wavy arrows illustrate the possible trajectories followed by oxidizing and volatile-rich,

slab-derived components (fluxing). Continuous and dotted black lines indicate the $C+O_2=CO_2$ (CCO) redox buffer, for hydrous and anhydrous conditions respectively (Ballhaus 1993). The bold solid arrow indicates decompression melting of mantle at constant $Fe^{3+}/\sum Fe_{spinel}$ (fluxed-melting; Ballhaus 1993; Ballhaus and Frost 1994; Parkinson and Arculus 1999). Thin dotted arrow indicates an isochemical melt decompression path following isobaric melting at depth (Kress and Carmichael 1991). Thin continuous arrows illustrate isochemical melt decompression paths at variable pressure during a mantle decompression scenario (Kress and Carmichael 1991). The range of $\Delta \log fO_2$(FMQ) for primitive island arc lavas from Jugo et al. (2010) and Evans et al. (2012) overlaps with that determined for picrite-boninite-andesite (PBA) from the peridotite dataset in this study and the literature (>FMQ+1; Klimm et al. 2015; Bénard et al. 2016a). (**b**) Same plot as in (**a**) but here illustrating the petrogenesis of low-degree, relatively reduced low-Ca boninite (LCB) in equilibrium with orthopyroxene-poor harzburgite and dunite (blue fields; Fig. 9c). Here $Fe^{3+}/\sum Fe_{spinel}$ is un-buffered and decreases as melting proceeds during decompression (second-stage melting), such as is observed in the residual Ritter samples in this study. The black wavy arrow indicates post-melting metasomatism of residual, pyroxene- and spinel-poor peridotite in the sub-arc mantle lithosphere (Amundsen and Neumann 1992; Brandon and Draper 1996; Woodland et al. 2006). (**c**) A cross-section of the West Bismarck subduction zone mantle below Ritter. The isotherms are from the temperature-dependent viscosity models of Manea et al. (2005), further adapted to the geometry of the West Bismarck Arc subduction zone (Fig. 1a; Abers and Roecker 1991) and the mantle lithosphere temperatures of sub-solidus re-equilibration of the peridotite xenoliths in this study (Table 1). Red and blue arrows illustrate the formation and possible ascent-paths of melts originally equilibrated with relatively oxidized, orthopyroxene-rich harzburgite residues, and relatively reduced, orthopyroxene-poor harzburgite-dunite residues, respectively.

Table 1. Petrological information on West Bismarck sub-arc mantle peridotites in this study

Sample	Site	Rock type	$Fe^{3+}/\sum Fe_{spinel}$ [a]	±	T (°C) [b]	±	$\Delta \log fO_2$[FMQ] [c]	±	$\Delta \log fO_2$[FMQ] [d]	±	Al_2O_3 (wt%)	FeO_t (wt%) [e]	MgO (wt%)	NiO (wt%)
Residual peridotite														
63-01(4)	*Cone 2*	*Harzburgite*	*0.23*	*0.03*	*709*	*19*	*1.51*	*0.28*	*1.23*	*0.26*	*0.55*	*7.42*	*46.01*	*0.31*
67-02A(2)	Cone 4	Harzburgite	0.19	0.01	804	3	0.58	0.14	0.20	0.11	0.41	7.68	47.39	0.34
67-02B(1)	Cone 4	Harzburgite	0.14	0.01	768	3	-0.03	0.16	-0.43	0.14	0.58	7.35	45.62	0.31
67-02B(3)	Cone 4	Harzburgite	0.16	0.01	817	3	0.15	0.16	-0.22	0.13	0.36	7.58	47.47	0.33
67-02B(7)	Cone 4	Harzburgite	0.15	0.01	717	1	0.15	0.17	-0.03	0.13	0.68	7.34	45.82	0.30
67-02D(1)	*Cone 4*	*Dunite*	*0.13*	*0.03*	*706*	*15*	*0.01*	*0.45*	*-0.24*	*0.42*	*0.29*	*8.32*	*46.90*	*0.31*
67-02D(7) [f]	*Cone 4*	*Harzburgite*	*0.29*	*0.04*	*903*	*27*	*1.48*	*0.28*	*1.03*	*0.24*	*0.52*	*7.84*	*47.54*	*0.34*
67-02E(1)	Cone 4	Harzburgite	0.11	0.01	721	2	-0.50	0.20	-0.83	0.17	0.37	8.26	47.51	0.34
67-02E(2)	Cone 4	Harzburgite	0.20	0.01	774	1	0.76	0.15	0.40	0.11	0.56	7.24	45.27	0.30
67-02E(5)	Cone 4	Harzburgite	0.26	0.01	730	2	1.46	0.12	1.15	0.08	0.72	7.57	45.35	0.30
67-02E(6)	*Cone 4*	*Harzburgite*	*0.27*	*0.04*	*789*	*24*	*1.73*	*0.24*	*1.37*	*0.23*	*0.47*	*7.27*	*46.24*	*0.31*
Melt channel-cumulate			0.01											
62-01(1)	Cone 1	Dunite	0.21	0.01	698	2	-	-	-	-	0.20	8.57	49.37	0.25
62-01(2)	*Cone 1*	*Dunite*	*0.21*	*0.03*	*671*	*16*	-	-	-	-	*0.17*	*7.18*	*50.28*	*0.24*
62-02(4)	*Cone 1*	*Dunite*	*0.19*	*0.03*	*667*	*15*	-	-	-	-	*0.11*	*8.33*	*49.67*	*0.20*

Sample	Olivine (wt%)	±	Opx (wt%)	±	Cpx (wt%)	±	Spinel (wt%)	±	Sum (wt%)	$Mg\#_{spinel}$ [g]	$Cr\#_{spinel}$ [h]	$Cr/(Cr+Al+Fe^{3+})_{spinel}$ [i]
Residual peridotite												
63-01(4)	*75.2*	*1.1*	*22.9*	*1.6*	*0.9*	*0.9*	*0.9*	*0.4*	*100*	*0.399*	*0.720*	*0.665*
67-02A(2)	77.2	0.8	21.2	1.1	1.1	0.6	0.5	0.3	100	0.550	0.563	0.537
67-02B(1)	75.1	0.8	22.7	1.1	1.5	0.6	0.6	0.3	100	0.555	0.553	0.536
67-02B(3)	86.4	1.1	12.3	1.5	1.1	0.8	0.2	0.4	100	0.570	0.562	0.542
67-02B(7)	72.6	0.5	25.1	0.7	1.3	0.4	0.9	0.2	100	0.531	0.520	0.501
67-02D(1)	*91.3*	*0.5*	*7.2*	*0.7*	*1.1*	*0.4*	*0.4*	*0.2*	*100*	*0.455*	*0.604*	*0.582*
67-02D(7) [f]	*84.8*	*0.7*	*13.2*	*1.0*	*1.0*	*0.6*	*1.0*	*0.2*	*100*	*0.542*	*0.665*	*0.614*
67-02E(1)	87.6	1.1	11.0	1.5	1.1	0.9	0.2	0.4	100	0.544	0.494	0.482
67-02E(2)	70.6	0.6	27.7	0.8	1.5	0.5	0.2	0.2	100	0.528	0.569	0.540
67-02E(5)	71.2	0.6	26.5	0.8	1.4	0.4	0.9	0.2	100	0.467	0.546	0.506
67-02E(6)	*75.2*	*0.5*	*22.9*	*0.7*	*0.7*	*0.4*	*1.2*	*0.2*	*100*	*0.419*	*0.761*	*0.694*
Melt channel-cumulate												
62-01(1)	98.9	0.3	-	-	0.3	0.3	0.8	0.2	100	0.339	0.760	0.704
62-01(2)	*98.8*	*0.3*	-	-	*0.3*	*0.3*	*1.0*	*0.2*	*100*	*0.299*	*0.889*	*0.813*
62-02(4)	*99.1*	*0.3*	-	-	-	-	*0.9*	*0.2*	*100*	*0.312*	*0.797*	*0.737*

Bulk rock and spinel major element compositions are from Bénard et al. (2017) and McAlpine (2016) respectively

Modal proportions are calculated by least-square regression of the XRF and EPMA data, respectively on bulk rocks and their minerals (Bénard et al. 2017)

[a] $Fe^{3+}/(Fe^{2+}+Fe^{3+})$ in spinel determined by Mössbauer spectroscopy (straight) or precise EPMA (italics)

[b] Temperatures calculated with the olivine-spinel geothermometer of Ballhaus et al. (1991) at 1.5 GPa

[c] fO_2 calculated using the olivine-spinel temperature of Ballhaus et al. (1991) and the oxybarometer of Wood et al. (1990) at 1.5 GPa

[d] fO_2 calculated using the olivine-spinel temperature and the oxybarometer of Ballhaus et al. (1991) at 1.5 GPa
[e] Total iron treated as ferrous oxide
[f] Sample with abundant silica-rich, chromite-hosted melt inclusions (Bénard et al. 2017)
[g] Mg/(Mg+∑Fe) in spinel (averages)
[h] Cr/(Cr+Al) in spinel (averages)
[i] Cr/(Cr+Al+Fe^{3+}) in spinel (averages)
Opx, orthopyroxene; cpx, clinopyroxene

Highlights

1. $\Delta\log fO_2$ in West Bismarck Arc mantle peridotites ranges from FMQ-0.5 to FMQ+1.7
2. $Fe^{3+}/\Sigma Fe_{spinel}$ and fO_2 correlate with bulk rock Al_2O_3 and orthopyroxene contents
3. The overall fO_2 range is modelled by a two-stage partial melting process
4. Oxidized picrite-boninite-andesite form by fluxed-melting
5. Relatively reduced low-Ca boninite form by adiabatic decompression melting

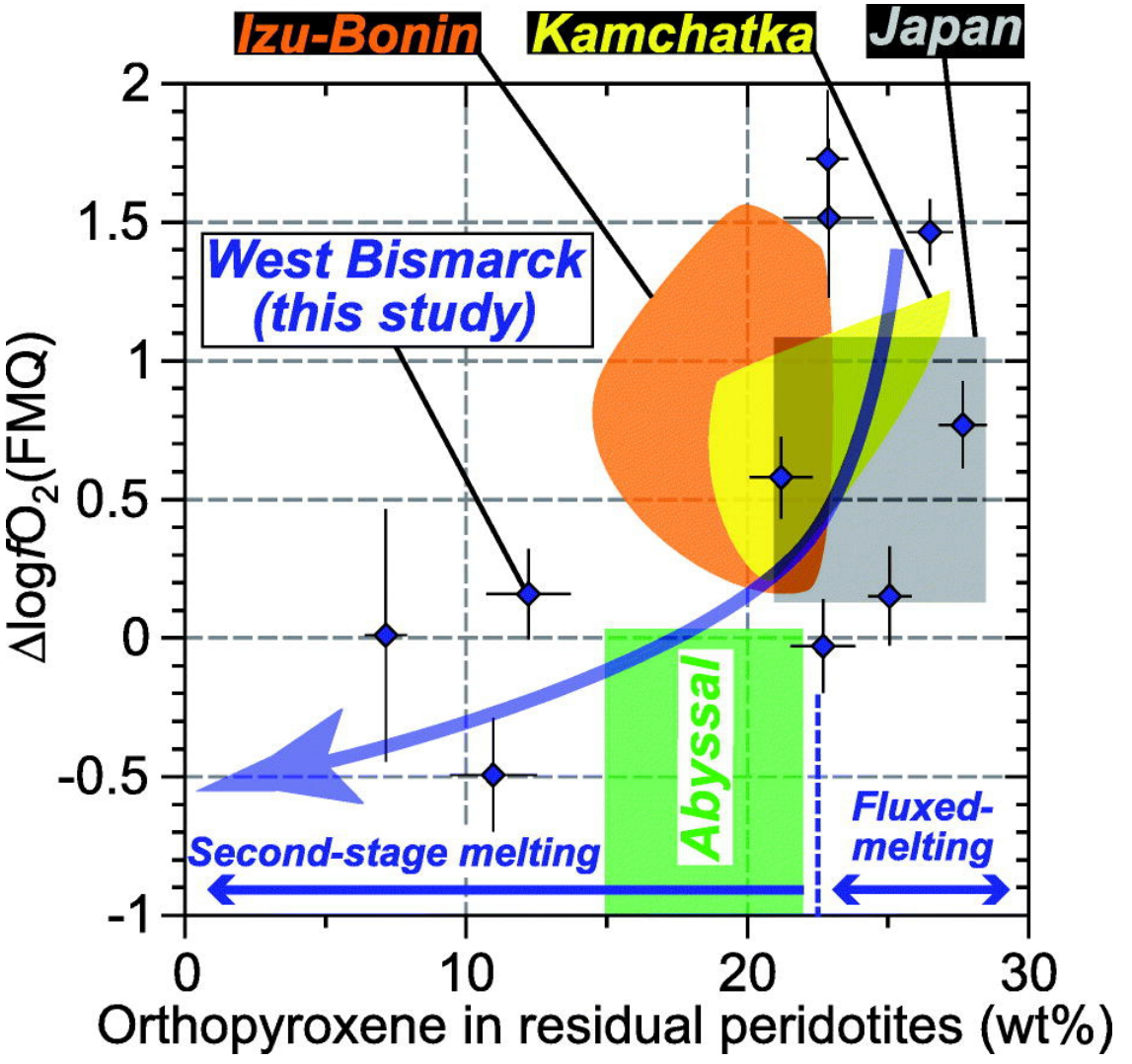

Graphics Abstract

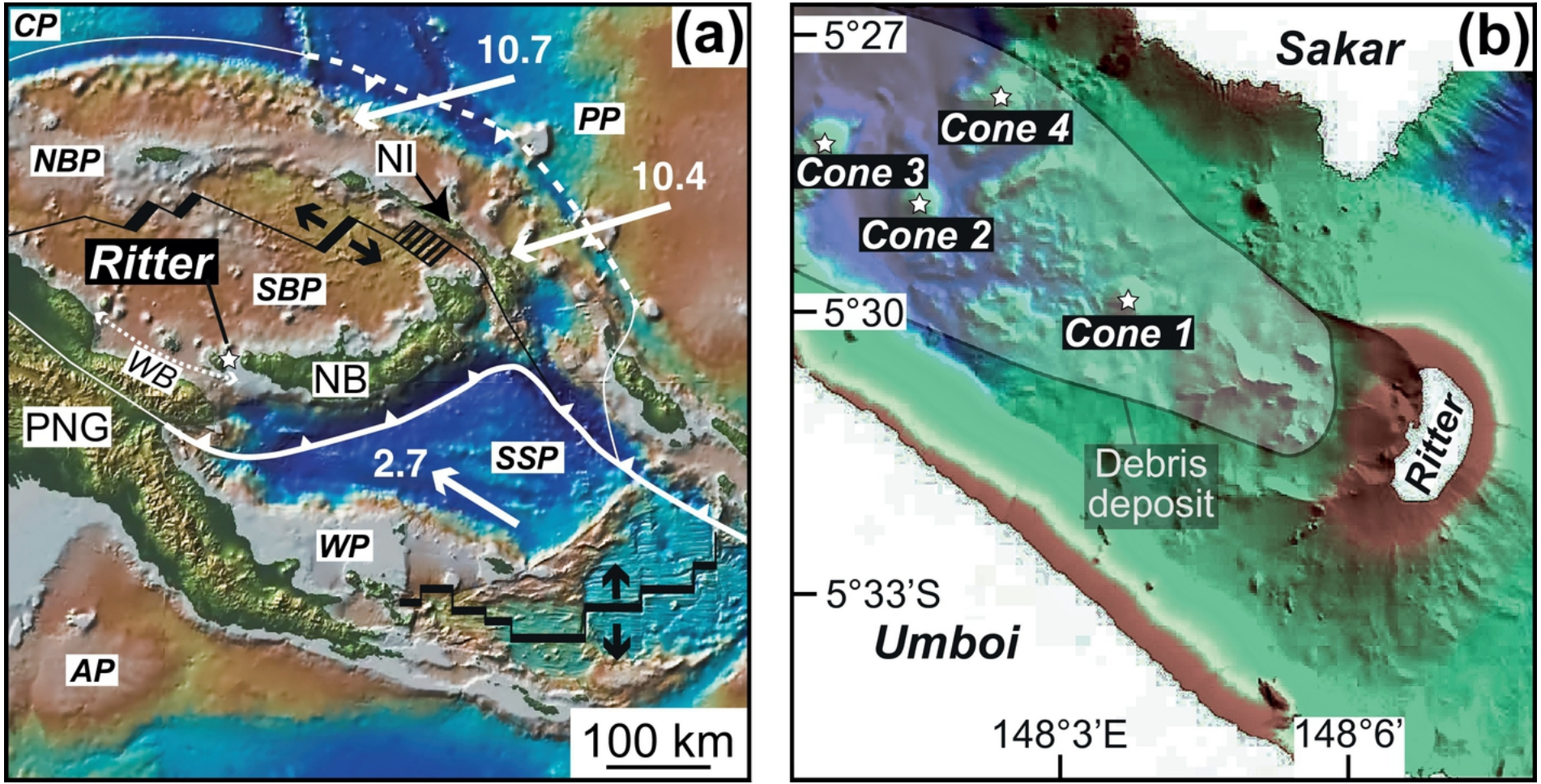
(a)
CP
10.7
PP
NBP
NI
10.4
Ritter
SBP
WB
NB
PNG
2.7
SSP
WP
AP
100 km
(b)
5°27
Sakar
Cone 4
Cone 3
Cone 2
5°30
Cone 1
Ritter
Debris
deposit
5°33'S
Umboi
148°3'E
148°6'

Figure 1

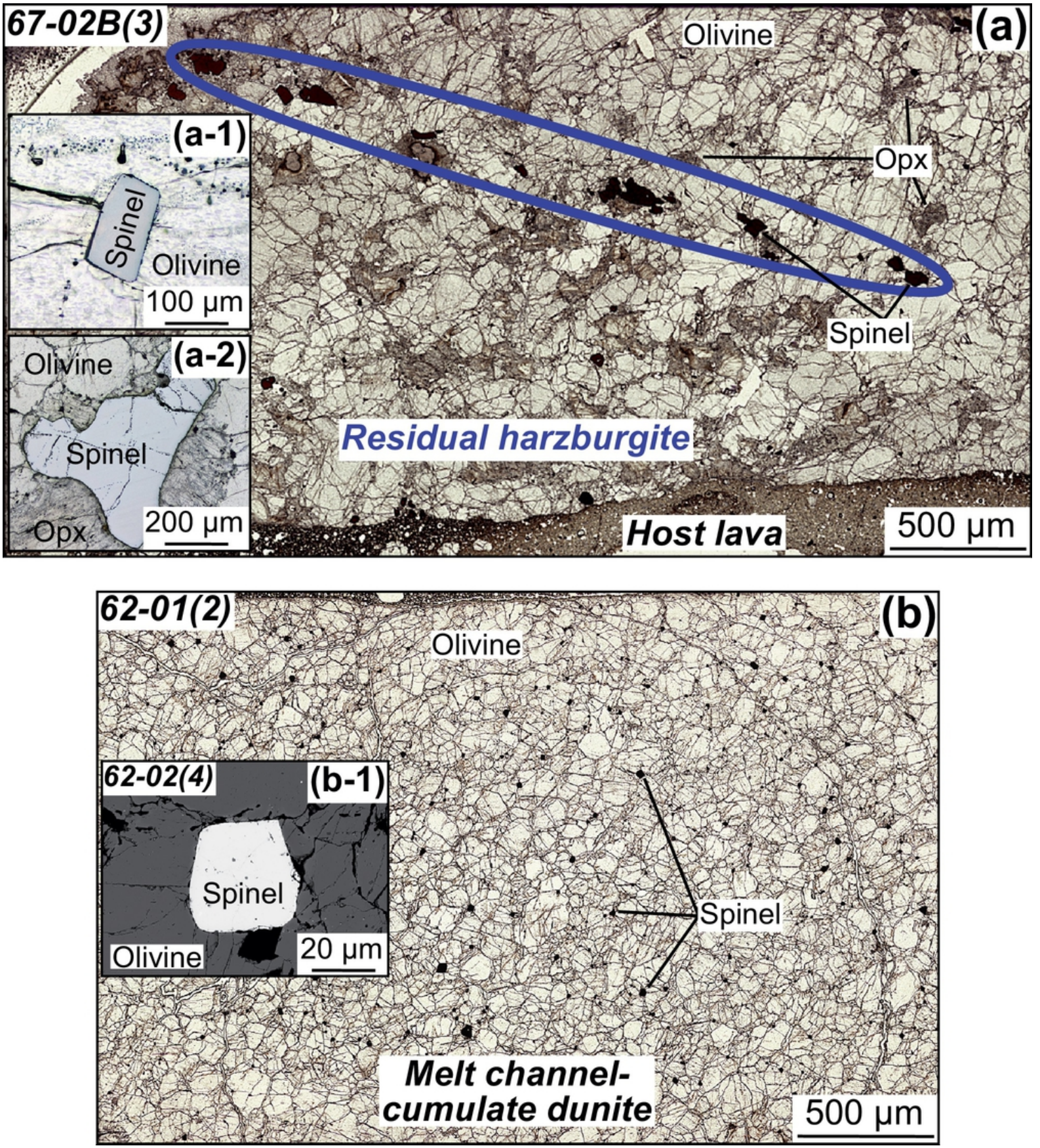
67-02B(3)
(a)
Olivine
Opx
Spinel
(a-1)
Spinel
Olivine
100 μm
(a-2)
Olivine
Spinel
Opx
200 μm
Residual harzburgite
Host lava
500 μm
62-01(2)
(b)
Olivine
62-02(4)
(b-1)
Spinel
Olivine
20 μm
Spinel
Melt channel-
cumulate dunite
500 μm

Figure 2

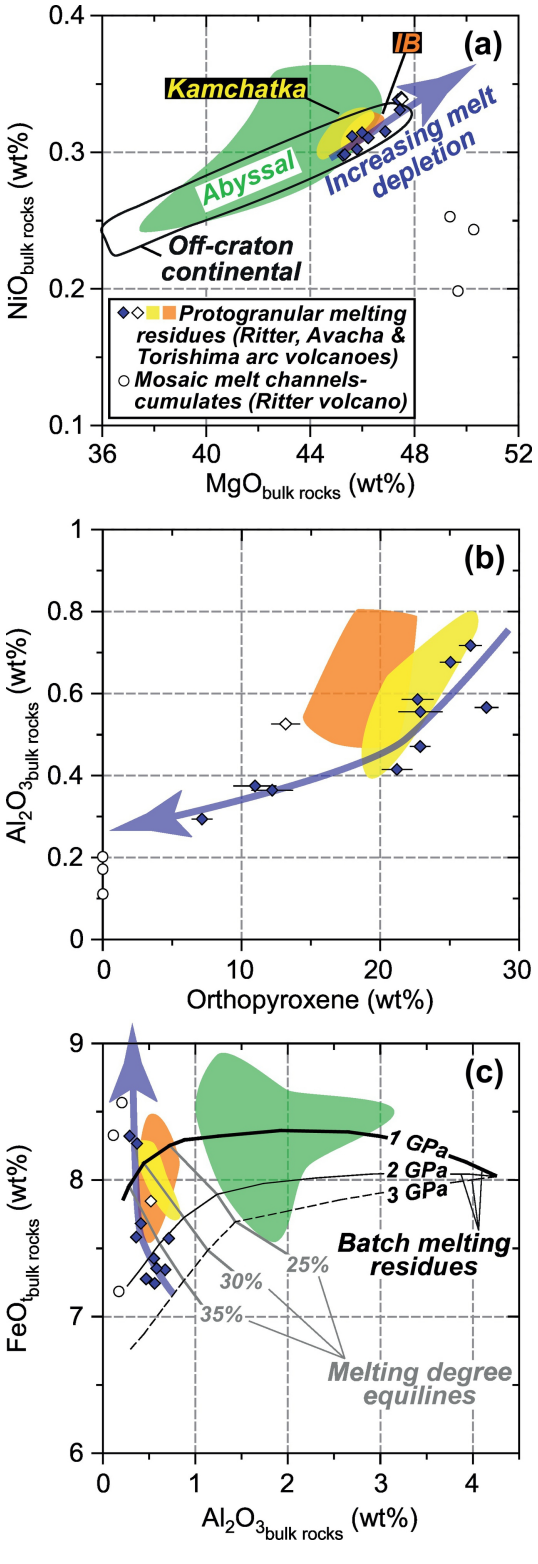
(a)
IB
Kamchatka
Abyssal
Increasing melt depletion
Off-craton continental
Protogranular melting residues (Ritter, Avacha & Torishima arc volcanoes)
Mosaic melt channels-cumulates (Ritter volcano)
NiO bulk rocks (wt%)
MgO bulk rocks (wt%)
0.4
0.3
0.2
0.1
36
40
44
48
52
(b)
Al2O3 bulk rocks (wt%)
Orthopyroxene (wt%)
1
0.8
0.6
0.4
0.2
0
0
10
20
30
(c)
1 GPa
2 GPa
3 GPa
Batch melting residues
25%
30%
35%
Melting degree equilines
FeO bulk rocks (wt%)
Al2O3 bulk rocks (wt%)
9
8
7
6
0
1
2
3
4

Figure 3

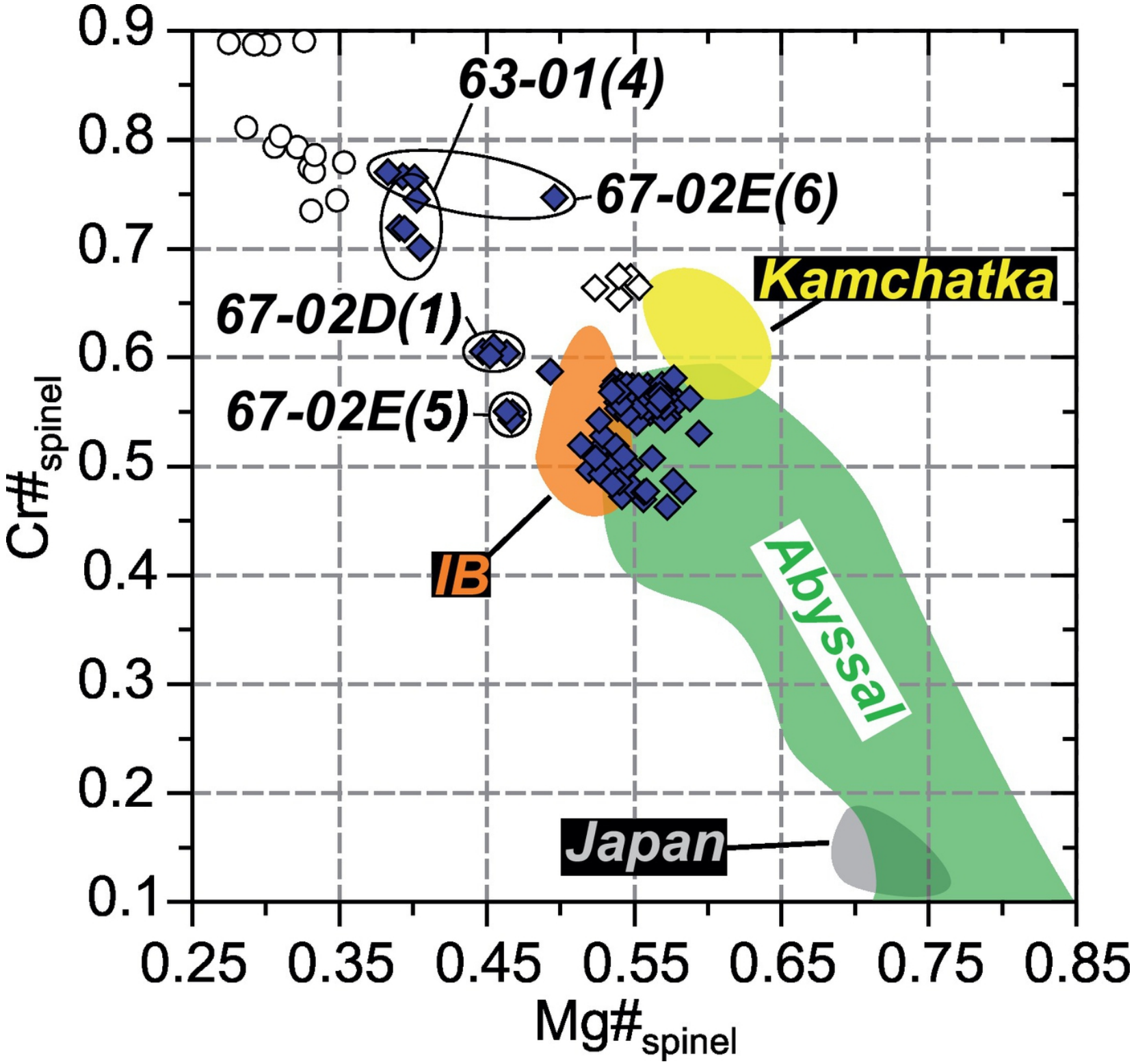
63-01(4)
67-02E(6)
67-02D(1)
67-02E(5)
Kamchatka
IB
Abyssal
Japan
Cr#spinel
Mg#spinel
0.9
0.8
0.7
0.6
0.5
0.4
0.3
0.2
0.1
0.25
0.35
0.45
0.55
0.65
0.75
0.85

Figure 4

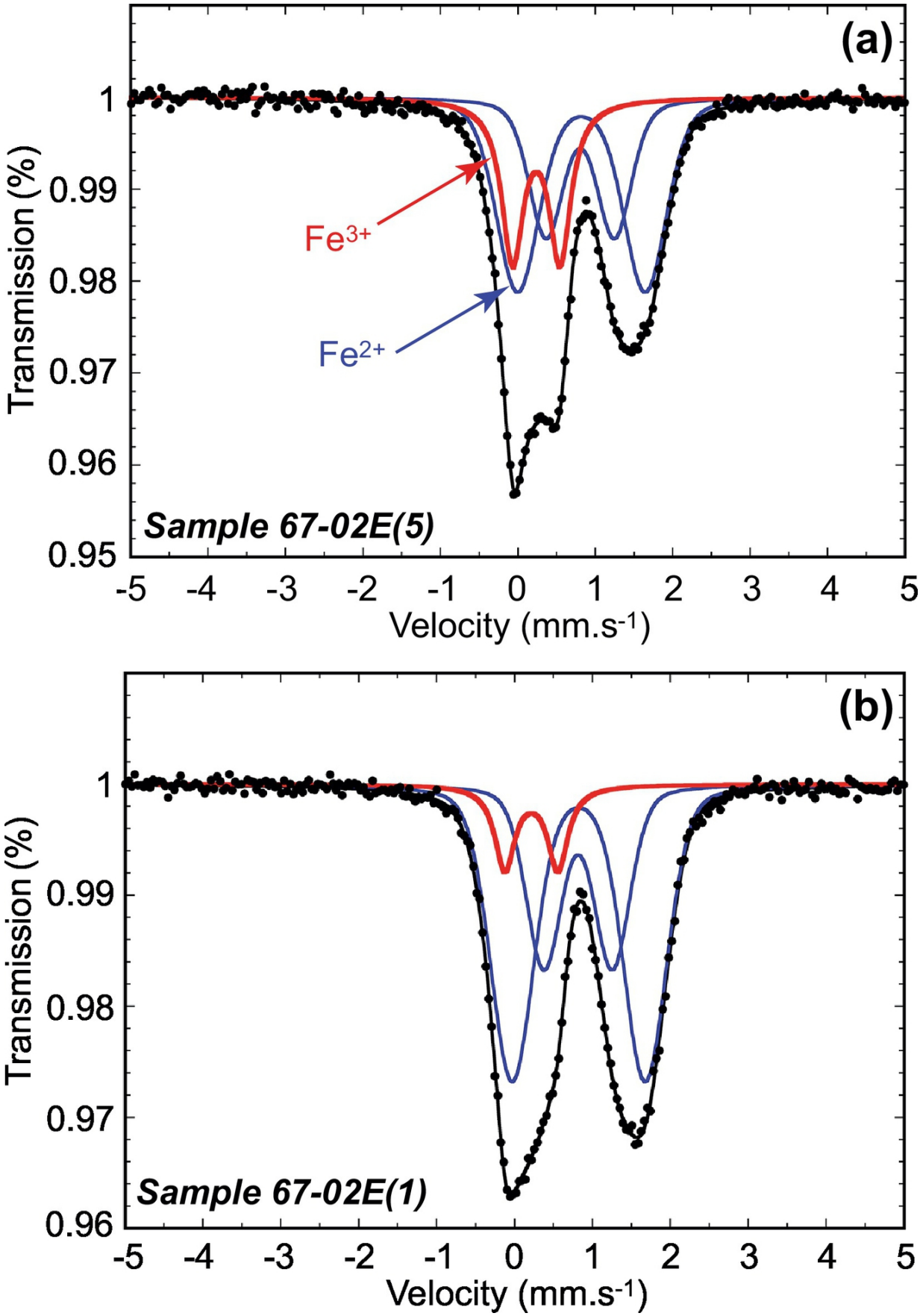
(a)
Transmission (%)
1
0.99
0.98
0.97
0.96
0.95
Fe3+
Fe2+
Sample 67-02E(5)
-5 -4 -3 -2 -1 0 1 2 3 4 5
Velocity (mm.s-1)
(b)
Transmission (%)
1
0.99
0.98
0.97
0.96
Sample 67-02E(1)
-5 -4 -3 -2 -1 0 1 2 3 4 5
Velocity (mm.s-1)

Figure 5

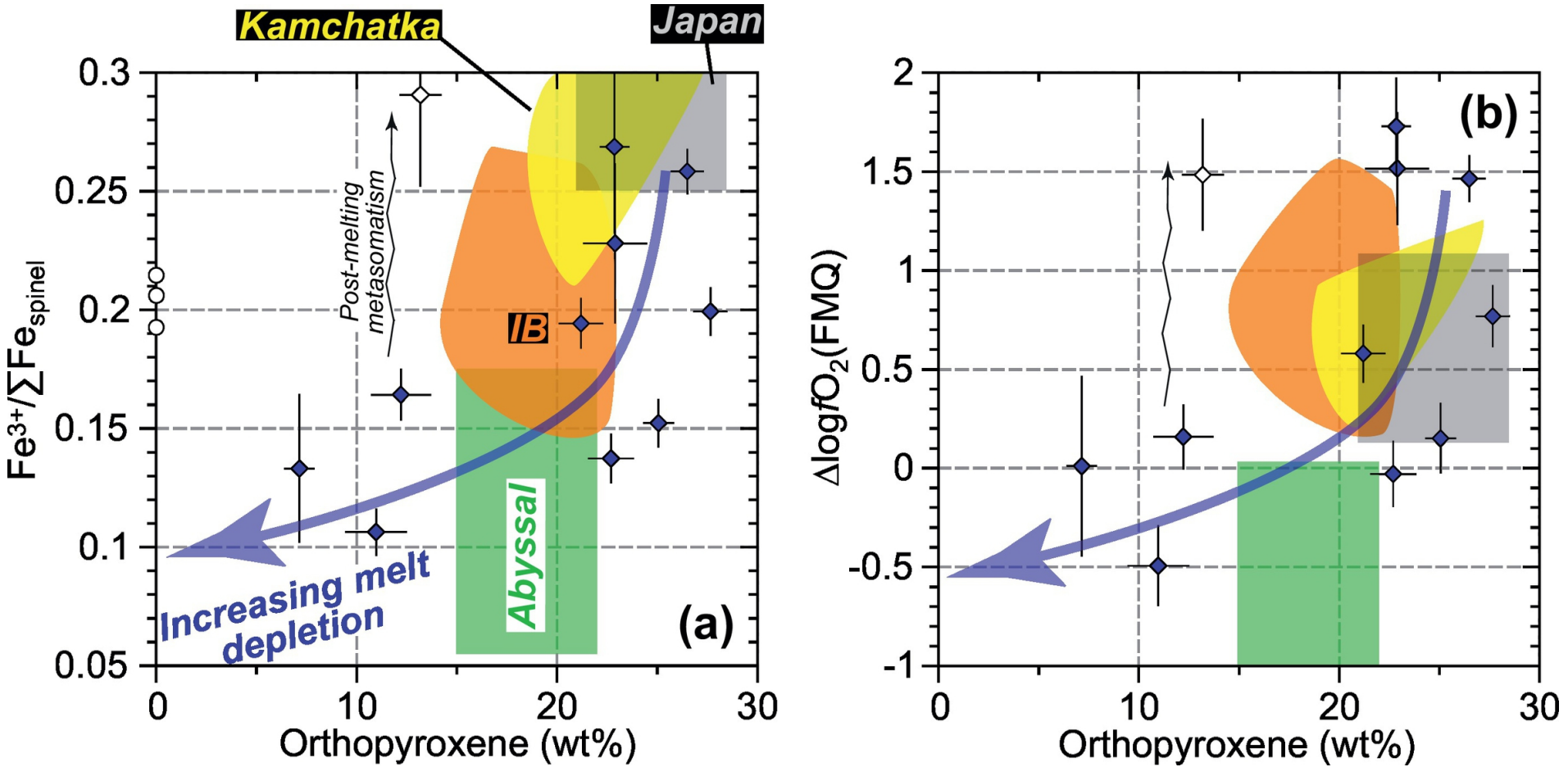
Kamchatka
Japan
Post-melting metasomatism
IB
Abyssal
Increasing melt depletion
(a)
(b)
Fe3+/∑Fespinel
ΔlogfO2(FMQ)
Orthopyroxene (wt%)
Orthopyroxene (wt%)

Figure 6

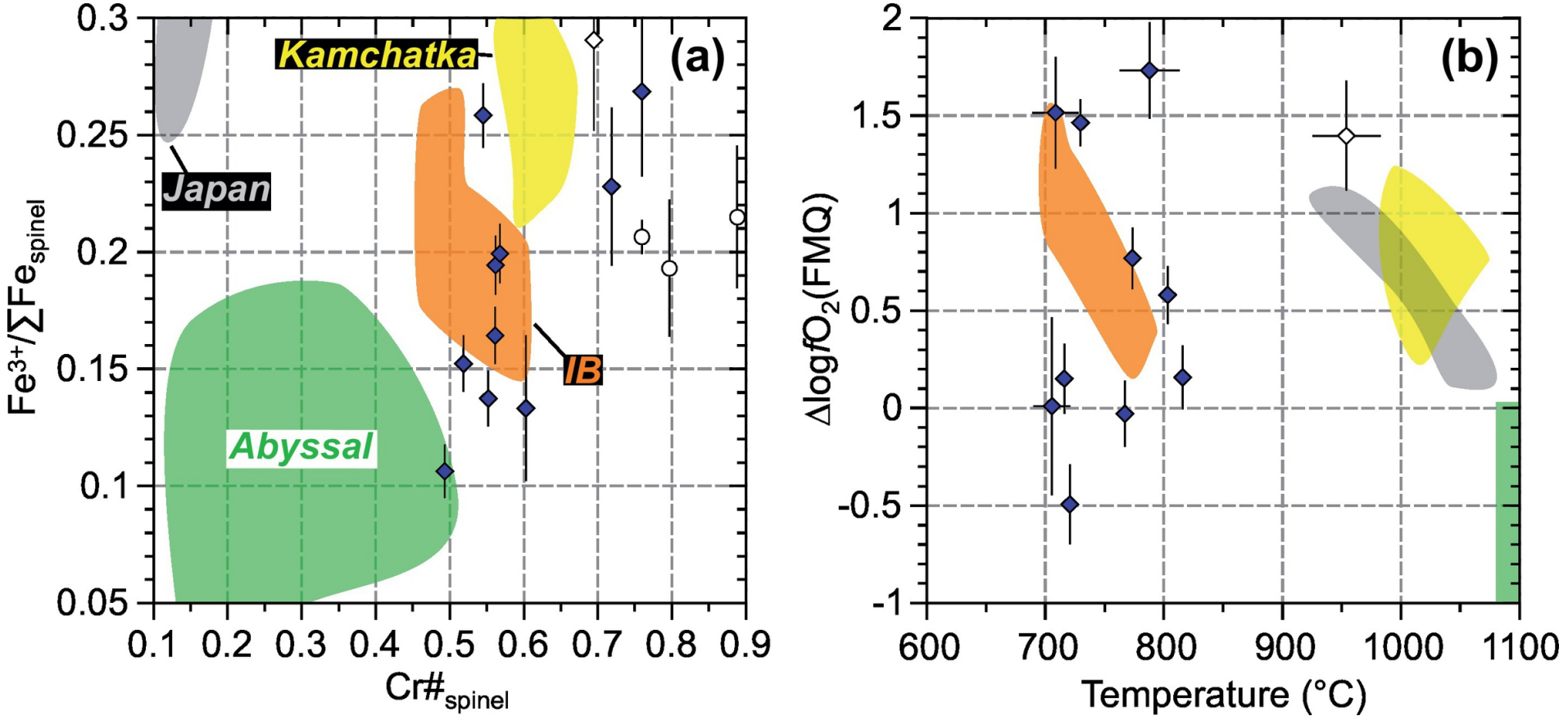
(a)
Kamchatka
Japan
IB
Abyssal
Fe3+/∑Fespinel
Cr#spinel
0.3
0.25
0.2
0.15
0.1
0.05
0.1 0.2 0.3 0.4 0.5 0.6 0.7 0.8 0.9
(b)
ΔlogfO2(FMQ)
Temperature (°C)
2
1.5
1
0.5
0
-0.5
-1
600 700 800 900 1000 1100

Figure 7

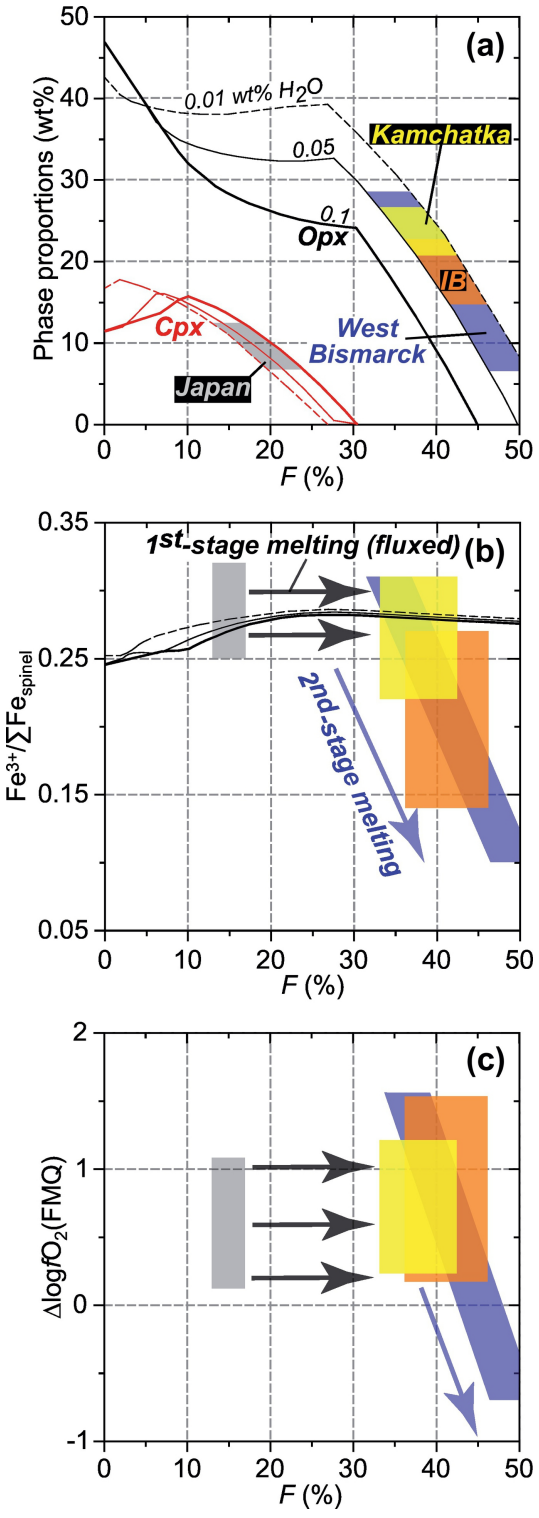
(a)
Phase proportions (wt%)
F (%)
0.01 wt% H2O
0.05
0.1
Opx
Cpx
Kamchatka
IB
West Bismarck
Japan
(b)
1st-stage melting (fluxed)
2nd-stage melting
Fe3+/∑Fespinel
(c)
ΔlogfO2(FMQ)

Figure 8

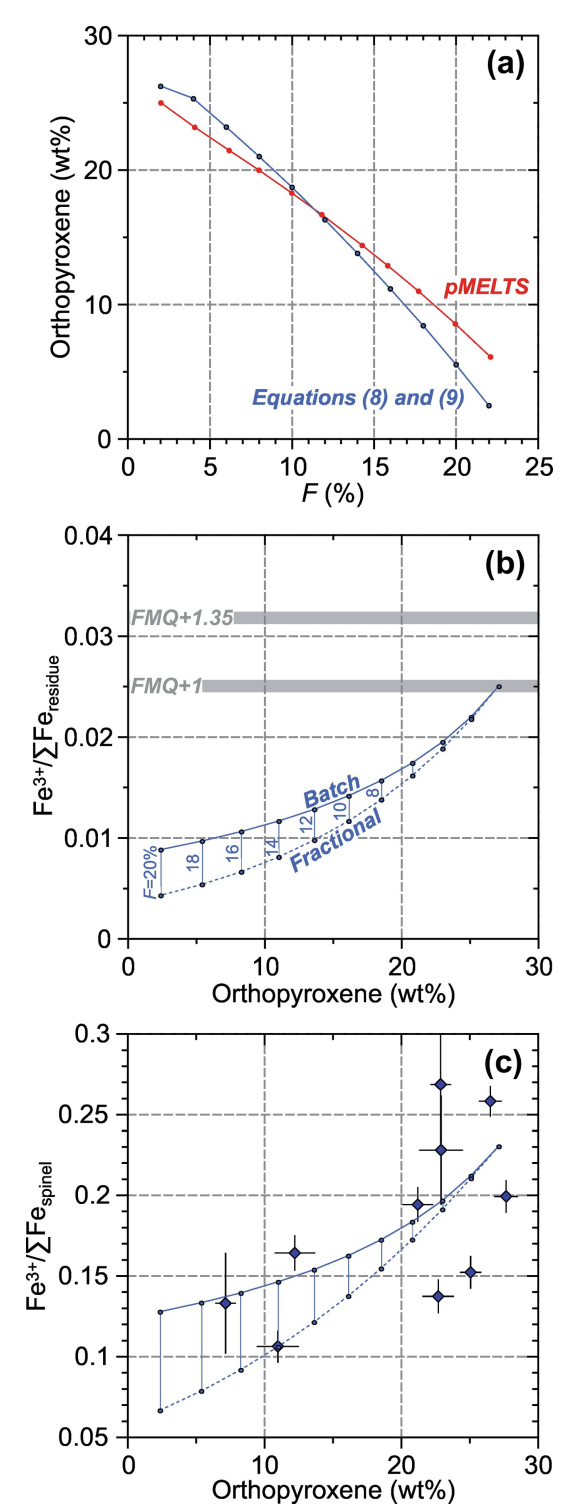
(a)
Orthopyroxene (wt%)
F (%)
pMELTS
Equations (8) and (9)
(b)
FMQ+1.35
FMQ+1
Batch
Fractional
F=20%
18
16
14
12
10
8
Fe3+/∑Fe residue
Orthopyroxene (wt%)
(c)
Fe3+/∑Fe spinel
Orthopyroxene (wt%)

Figure 9

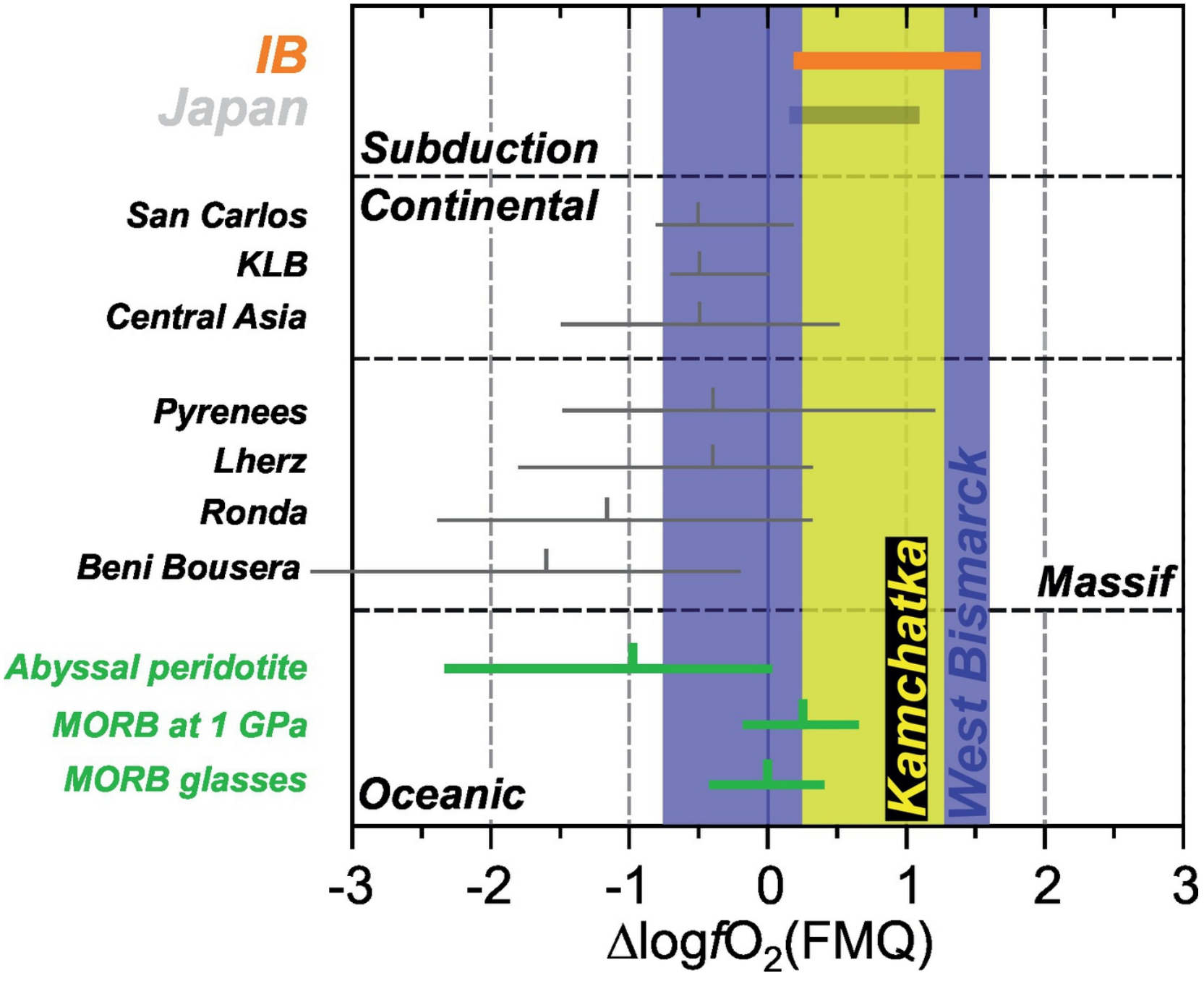
IB
Japan
Subduction
Continental
San Carlos
KLB
Central Asia
Pyrenees
Lherz
Ronda
Beni Bousera
Massif
Abyssal peridotite
MORB at 1 GPa
MORB glasses
Oceanic
Kamchatka
West Bismarck
-3
-2
-1
0
1
2
3
ΔlogfO2(FMQ)

Figure 10

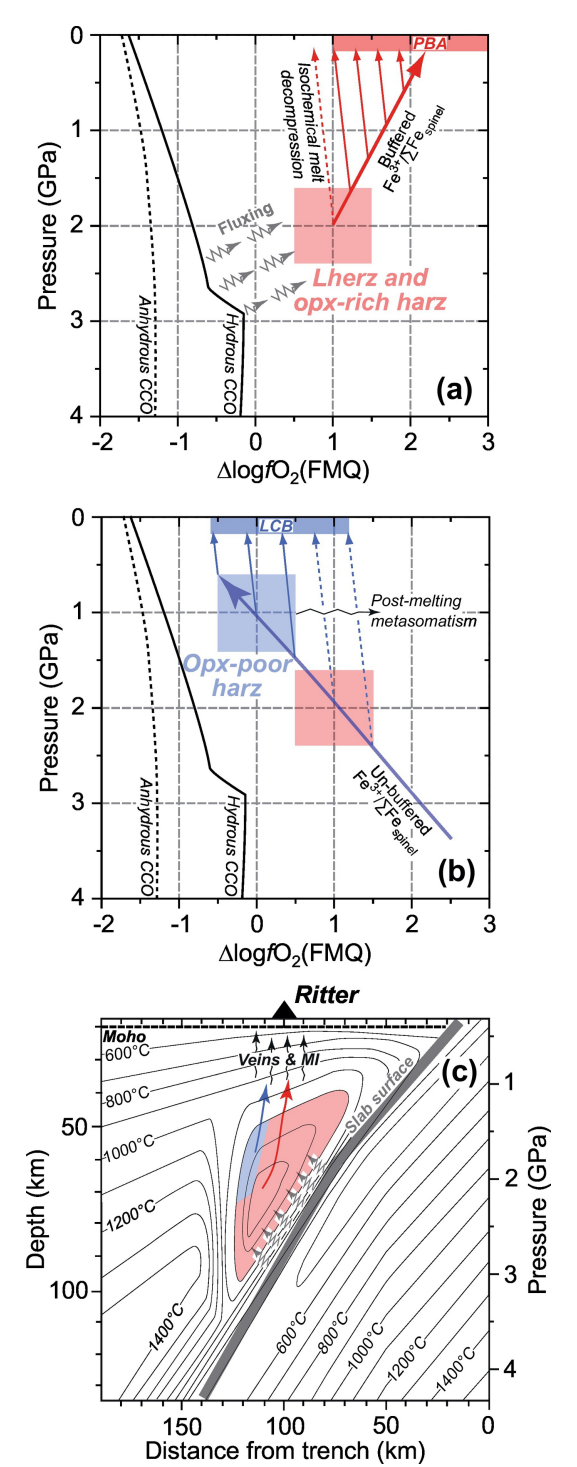
PBA
Isochemical melt decompression
Buffered Fe3+/ΣFespinel
Fluxing
Lherz and opx-rich harz
Anhydrous CCO
Hydrous CCO
(a)
Pressure (GPa)
ΔlogfO2(FMQ)
LCB
Post-melting metasomatism
Opx-poor harz
Un-buffered Fe3+/ΣFespinel
(b)
Ritter
Moho
600°C
800°C
1000°C
1200°C
1400°C
Veins & MI
Slab surface
(c)
Depth (km)
Pressure (GPa)
Distance from trench (km)

Figure 11

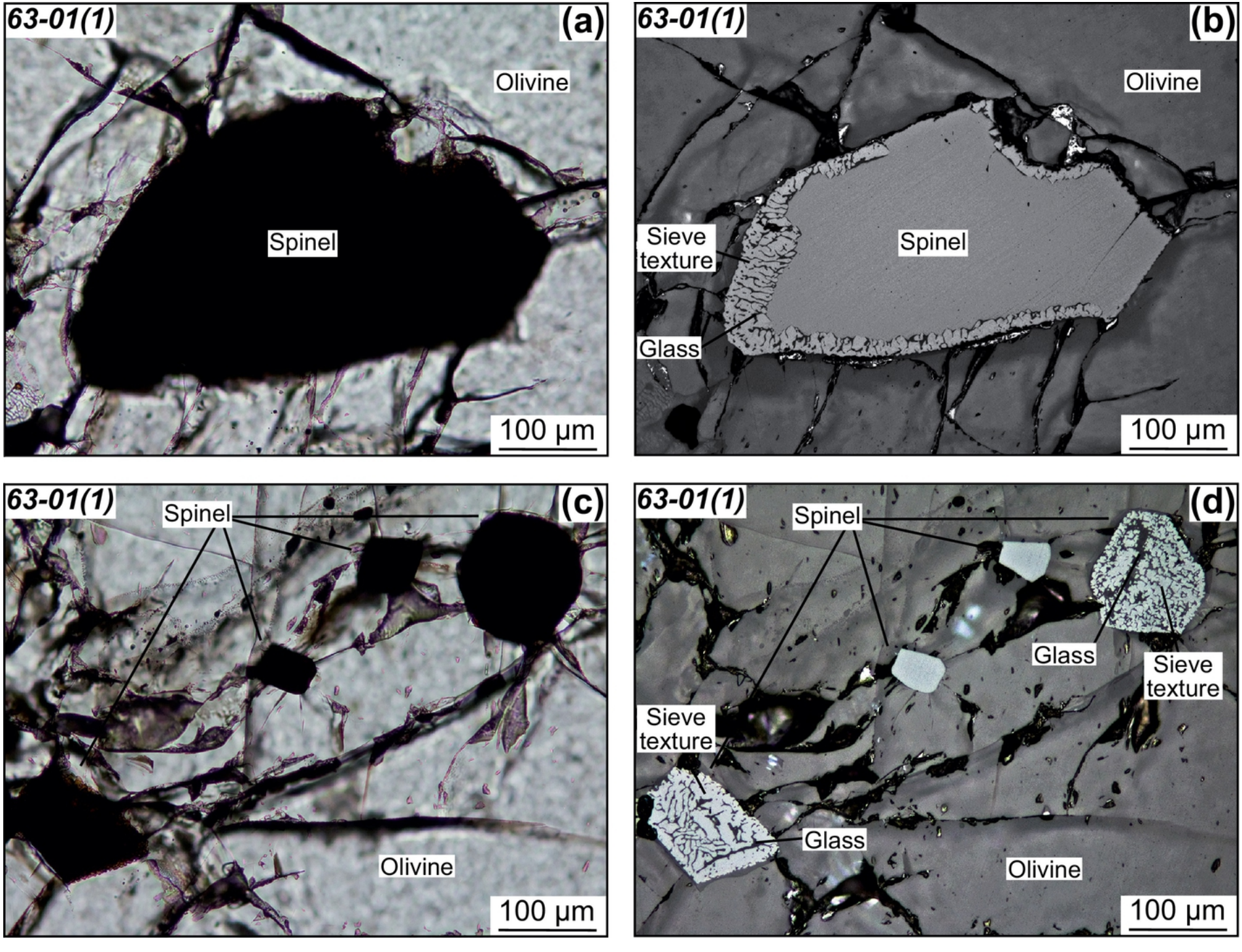
63-01(1)
(a)
Olivine
Spinel
100 µm
63-01(1)
(b)
Olivine
Sieve texture
Spinel
Glass
100 µm
63-01(1)
(c)
Spinel
Olivine
100 µm
63-01(1)
(d)
Spinel
Glass
Sieve texture
Sieve texture
Glass
Olivine
100 µm

Figure 12

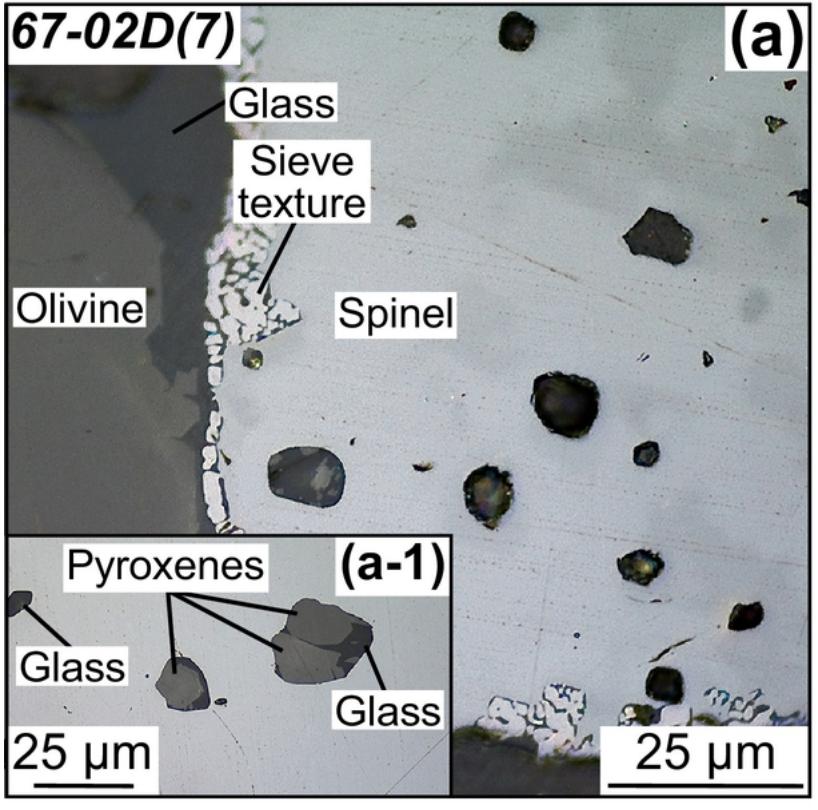
67-02D(7)
(a)
Glass
Sieve texture
Olivine
Spinel
Pyroxenes
(a-1)
Glass
Glass
25 µm
25 µm

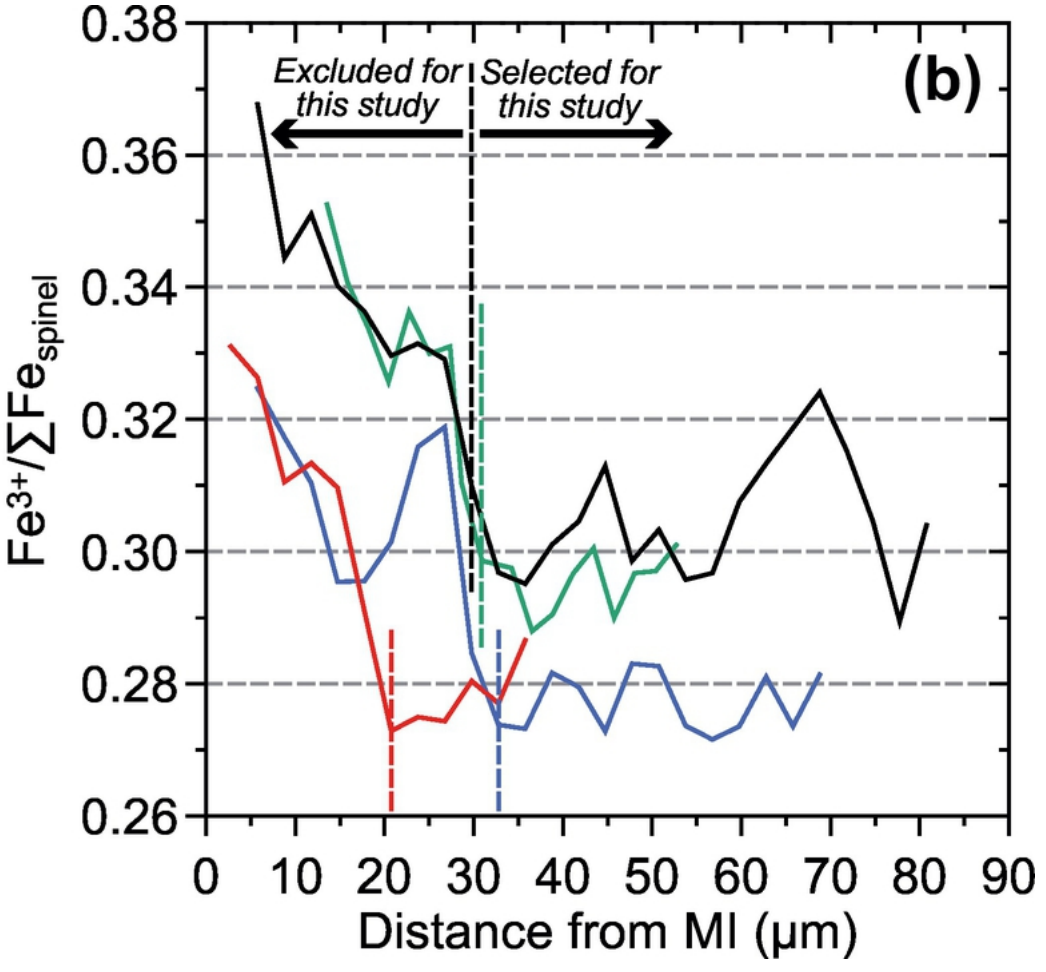
(b)
Excluded for this study
Selected for this study
Fe3+/∑Fespinel
0.38
0.36
0.34
0.32
0.30
0.28
0.26
0
10
20
30
40
50
60
70
80
90
Distance from MI (µm)

Figure 13